



1 **Seasonal characteristics of emission, distribution, and radiative effect of marine organic aerosols**
2 **over the western Pacific Ocean: an investigation with a coupled regional climate-aerosol model**

3

4 Jiawei Li¹, Zhiwei Han^{1,2*}, Pingqing Fu³, Xiaohong Yao⁴

5

6 ¹CAS Key Laboratory of Regional Climate-Environment for Temperate East Asia (RCE-TEA),

7 Institute of Atmospheric Physics, Chinese Academy of Sciences, Beijing 100029, China

8 ²University of Chinese Academy of Sciences, Beijing 100049, China

9 ³School of Earth System Science, Tianjin University, Tianjin 300072, China

10 ⁴Laboratory of Marine Environmental Science and Ecology, Ministry of Education, Ocean University

11 of China, Qingdao 266100, China

12

13

14 Correspondence to: Zhiwei Han (hzw@mail.iap.ac.cn)

15

16 **Abstract:** Organic aerosols from marine sources over the western Pacific Ocean of East Asia were
17 investigated by using an online-coupled regional chemistry-climate model RIEMS-Chem for the
18 entire year 2014. Model evaluation against a wide variety of observations from research cruises and
19 in-situ measurements demonstrated a good skill of the model in simulating temporal variation and
20 spatial distribution of particulate matter with aerodynamic diameter less than 2.5 μm and 10 μm
21 ($\text{PM}_{2.5}$ and PM_{10}), black carbon (BC), organic carbon (OC), sodium, and aerosol optical depth (AOD)
22 in the marine atmosphere. The inclusion of marine organic aerosols apparently improved model
23 performance on OC aerosol concentration. The regional and annual mean near surface marine organic
24 aerosol (MOA) concentration was estimated to be 0.27 $\mu\text{g m}^{-3}$, with the maximum in spring and the
25 minimum in winter and contributed 26% of the total organic aerosol concentration on average over the
26 western Pacific. Marine primary organic aerosol (MPOA) accounted for the majority of marine
27 organic aerosol (MOA) mass and exhibited the maximum in autumn and the minimum in summer,
28 whereas marine secondary organic aerosol (MSOA) was approximately 1~2 orders of magnitude
29 lower than MPOA, having a distinct summer maximum and a winter minimum. MOA induced a direct
30 radiative effect (DRE_{MOA}) of -0.27 W m^{-2} , and an indirect radiative effect (IRE_{MOA}) of -0.66 W m^{-2} at



31 TOA (IRE_{MOA}) in terms of annual and oceanic average over the western Pacific, with the highest
32 seasonal mean IRE_{MOA} up to -0.94 W m^{-2} in spring. IRE_{MOA} was stronger than but in a similar
33 magnitude to the IRE due to sea salt aerosol on average, and it was approximately 9% of the IRE due
34 anthropogenic aerosols in terms of annual mean over the western Pacific, and this ratio increased to 19%
35 in the northern parts of the western Pacific in autumn. This study reveals an important role of MOA in
36 perturbing cloud properties and shortwave radiation fluxes in the western Pacific of East Asia.

37

38 **1 Introduction**

39 Atmospheric aerosol is one of the most important and uncertain factors in climate change issues
40 (IPCC, 2013). Aerosols can alter radiation balance by scattering/absorbing solar/infrared radiation,
41 and affect cloud microphysics and lifetime by activating as cloud condensation nuclei (CCN), exerting
42 significant effects on climate system directly and indirectly. Aerosols are originated from
43 anthropogenic and natural sources and of high spatial and temporal variability and short atmospheric
44 lifetime relative to greenhouse gases. Consequently, aerosol radiative and climatic effects often have
45 strong regional characteristics.

46 The western Pacific Ocean is frequently influenced by continental outflow of both anthropogenic
47 and natural aerosols. Due to continuous growth of economy and energy consumption in the past
48 decades, the aerosol level in China has been enhanced (Smith et al., 2011; Li M. et al., 2017) and may
49 have potentially significant effects on radiation and cloud over not only the East Asian continent but
50 also the wide downwind oceanic areas. Besides, East Asia is one of the major dust source regions on
51 earth (Shao and Dong, 2006). Dust storms often occur in spring and dust particles can be transported
52 eastward from the deserts and Gobi areas of north China and southern Mongolia to the western Pacific
53 Ocean (Gong et al., 2003), providing nutrients (e.g., iron) for phytoplankton or even triggering the
54 outbreak of algae bloom in oceans (Calil et al., 2011; Tan et al., 2017). In addition to anthropogenic
55 and dust aerosols, marine aerosols also significantly affect aerosol chemical composition, radiation
56 transfer, and cloud properties in marine atmosphere. The behaviors and climatic impacts of sea salt
57 and non-sea-salt sulfate oxidized from dimethylsulphide (DMS) have been extensively investigated
58 (Graf et al., 1997; Liao et al., 2004; Rap et al., 2013). In recent years, particular attentions have been
59 paid on the sources and impacts of marine organic aerosols (O'Dowd et al., 2004; Meskhidze and
60 Nenes, 2006; Luo and Yu, 2010; Vignati et al., 2010; Gantt et al., 2011; Burrow et al., 2014; Quinn et



61 al., 2017; Bertram et al., 2018; Huang et al., 2018), however, such studies were still very limited,
62 especially for the western Pacific.

63 O'Dowd et al. (2004) found that organic matter dominated the chemical composition of marine
64 aerosol during plankton bloom periods from spring to autumn over the North Atlantic Ocean,
65 contributing 63% to sub-micron aerosol mass. Meshkidze and Nenes (2006) revealed a significant
66 impact of phytoplankton bloom on cloud droplet number concentration and radiation balance in the
67 Southern Ocean and proposed a major contribution of secondary organic aerosol (SOA) from
68 phytoplankton produced isoprene. Some studies indicated that primary marine sources may dominate
69 marine organic matter, whereas SOA oxidized from marine isoprene could only comprise a small
70 fraction of the observed organic aerosol mass over marine environment (Facchini et al. 2008; Arnold
71 et al., 2009; Myriokefalitakis et al., 2010). The estimated global emission amounts of primary marine
72 organic matter varied largely among models. Using the global aerosol-climate model ECHAM5-HAM,
73 Roelofs (2008) estimated a global production of marine organic aerosols to be 75 TgC yr⁻¹. Spracklen
74 et al. (2008) estimated the marine organic carbon emission to be approximately 8 TgC yr⁻¹ based on
75 measured organic carbon mass and satellite retrieved chlorophyll-a (Chl-a) concentration. Vignati et al.
76 (2010) derived a global emission of marine primary organic matter in the sub-micron size by sea spray
77 process to be 5.8 TgC yr⁻¹ by using an off-line global Chemistry-Transport Model TM5 with a
78 parameterization relating organic emission fraction to sea surface Chl-a concentration. Gantt et al.
79 (2011) found that the combination of 10 m wind speed and sea surface Chl-a concentration were the
80 most consistent predictors of organic mass fraction of sea spray aerosol based on observations from
81 the Mace Head atmospheric research station on the Atlantic coast of Ireland and a site at the Point
82 Reyes National Seashore on the Pacific coast of California. They developed a new MPOA emission
83 function and estimated the global annual MPOA emission associated with sea spray to be from 15.9
84 TgC yr⁻¹ to 18.7 TgC yr⁻¹ (2.8~5.6 TgC yr⁻¹ in the sub-micron size). However, Quinn et al. (2014)
85 found that the organic carbon content of sea spray aerosol is weakly correlated with satellite retrieved
86 chlorophyll-a concentration based on cruise measurements in the North Atlantic Ocean and the coastal
87 waters of California. Bates et al (2020) reported that plankton bloom has little effect on the emission
88 flux, organic fraction or cloud condensation nuclei of sea spray aerosol based on cruise experiment
89 over the North Atlantic. Burrows et al. (2014) developed a novel physically based framework for
90 parameterizing the organic fractionation of sea spray aerosol by consideration of ocean



91 biogeochemistry processes, and their predicted relationships between Chl-a and organic fraction are
92 similar to existing empirical parameterizations associated with ocean Chl-a concentrations at high
93 Chl-a levels, but the empirical relationships may not be adequate to predict OM fraction of sea spray
94 aerosol outside of strong seasonal blooms. Considering the strong bloom seasonality in the western
95 Pacific region and the availability of global satellite data for Chl-a concentration, and the lack of
96 cruise measurements on the relationship between sea spray organic aerosol fluxes and Chl-a in this
97 region, we adopted the scheme of Gantt et al (2011) for parameterizing marine primary organic
98 aerosol emission in this study.

99 Regarding the influence on climatic factors, such as cloud condensation nuclei (CCN),
100 Ovadnevaite et al. (2011) revealed that MPOA was a dichotomy of low hygroscopicity and high CCN
101 activity through analysis of ambient measurements of aerosol chemical compositions and size
102 distributions at the Mace Head atmospheric research station, and highlighted the importance of MPOA
103 in CCN activation over marine atmosphere. A later study of Westervelt et al. (2012) indicated that
104 marine organic aerosols was able to increase CCN by up to 50% in the Southern Ocean and by 3.7%
105 globally during the austral summer based on the model simulation of GISS GCM II'. Based on the
106 measurements from seven research cruises over the Pacific, Southern, Arctic, and Atlantic oceans
107 between 1993 and 2015, Quinn et al. (2017) indicated that sea spray aerosol generally makes a
108 contribution of less than 30% to CCN population at supersaturation of 0.1 to 1.0% on a global basis.
109 Burrows et al. (2022) pointed out that sea spray organic aerosol strengthened shortwave radiative
110 cooling by clouds by -0.36 W m^{-2} in the global annual mean, with the zonal mean contribution
111 exceeding -3.5 W m^{-2} in the Southern Ocean in summertime.

112 The above studies reveal the important role of marine organic aerosols in chemical composition,
113 radiation budget, and cloud microphysics with focus on the global scale. However, there is very
114 limited modeling research on this important and challenging issue for the western Pacific Ocean of
115 East Asia. To our knowledge, only two of our previous studies explored the effects of MPOA on
116 chemical composition, radiation, cloud and precipitation over the western Pacific in springtime with
117 an online-coupled regional chemistry/aerosol-climate model RIEMS-Chem (Han et al., 2019; Li et al.,
118 2019), whereas the seasonality and annual aspect of MPOA and MSOA produced by marine isoprene
119 and terpene are still unknown. In this study, we conducted a one-year simulation with the developed
120 RIEMS-Chem to further explore the characteristics and radiative impacts of marine organic aerosols



121 over the western Pacific. The model simulated aerosol compositions were validated against a wide
122 series of observations from ground and cruise measurements, and the simulated MSOA was evaluated
123 by comparison with cruise measured secondary organic tracer in marine air masses. To our knowledge,
124 for the first time, the seasonality of emissions, concentrations, direct and indirect radiative effects of
125 marine organic aerosols was characterized and the annual means were estimated specifically for the
126 western Pacific and for the key oceanic regions of concern over East Asia. This study would provide
127 new insights into properties and impacts of marine organic aerosols over the western Pacific and
128 would be a necessary supplement to the global perspective of marine organic aerosols.

129

130 2 Model and data

131 2.1 Model description and key processes

132 An online-coupled regional atmospheric chemistry/aerosol-climate model RIEMS-Chem was
133 used to investigate marine organic aerosols in this study. RIEMS-Chem composes of the host regional
134 climate model RIEMS (Fu et al., 2005; Xiong et al., 2009; Wang S.Y. et al., 2015) and a
135 comprehensive atmospheric chemistry/aerosol module. RIEMS was developed based on the dynamic
136 structure of the fifth-generation Pennsylvania State University NCAR Mesoscale Model (MM5; Grell
137 et al., 1995) with a series of parameterizations to represent major physical processes, such as a
138 modified Biosphere-Atmosphere Transfer Scheme (BATS; Dickinson et al., 1993) for land-surface
139 process, the Medium-Range Forecasts scheme (MRF; Hong and Pan, 1996) for planetary boundary
140 layer process, the Grell cumulus convective parameterization scheme (Grell, 1993) for convective
141 process, the Reisner explicit moisture scheme (Reisner et al., 1998) and a modified radiation package
142 of the NCAR Community Climate Model (CCM3; Kiehl et al., 1996) for radiation transfer processes
143 with aerosol effect. RIEMS has participated in the Regional Climate Model Intercomparison Project
144 (RMIP) for Asia and it was one of the best models in predicting surface air temperature and
145 precipitation over East Asia (Fu et al., 2005).

146 Atmospheric chemistry/aerosol modules have been incorporated into RIEMS in recent years,
147 establishing the online-coupled model RIEMS-Chem, which can account for the interactions among
148 chemistry, radiation, cloud, and meteorology (Han, 2010; Han et al., 2012). RIEMS-Chem has been
149 successfully applied in previous modeling studies on anthropogenic aerosols, mineral dust and marine
150 aerosols regarding spatial-temporal distributions, physical and chemical evolutions, and radiative and



151 climatic effects over East Asia (Han et al., 2012; 2013; 2019; Li et al., 2014; 2016a; 2016b; 2019;
152 2020). It is now participating in the international model comparison project MICS-Asia III (Model
153 Inter Comparison Study for Asia phase III) and shows a good ability in predicting aerosol
154 concentrations and AOD over East Asia (Gao et al., 2018).

155 RIEMS-Chem includes atmospheric chemistry and aerosol processes, such as gas and aqueous
156 phase chemistries which are represented by the CB-IV mechanism (Gery et al. 1989) and RADM
157 scheme (Chang et al., 1987), respectively; Sulfate is mainly produced from the oxidation of SO₂ by
158 OH radical in gas phase and the oxidation of dissolved SO₂ by H₂O₂, O₃, and metal catalysis in
159 aqueous phase (Chang et al., 1987). Nitrate and ammonium are produced through thermodynamic
160 processes represented by the ISORROPIA II model (Fountoukis and Nenes, 2007). BC, POA, and
161 anthropogenic primary PMs are considered chemically inert. SOA formation from anthropogenic and
162 biogenic VOC precursors is treated by a bulk yield scheme from Lack et al. (2004), with SOA yield of
163 424 μg m⁻³ ppm⁻¹ for toluene, 342 μg m⁻³ ppm⁻¹ for xylene, and 762 μg m⁻³ ppm⁻¹ for monoterpene.
164 For irreversible conversion of marine VOCs to SOA, a 28.6% mass yield is assumed for isoprene
165 (Surratt et al., 2010, Meskhidze et al., 2011) and 30% for monoterpene (Lee et al., 2006).
166 Heterogeneous reactions between gaseous precursors and aerosols are also taken into account (Li and
167 Han, 2010; Li J. W. et al., 2018). Dry deposition velocity is represented by a size-dependent
168 parameterization over different underlying surfaces (Han et al., 2004). Dry deposition velocity of
169 particle is expressed as the inverse of the sum of resistant plus a gravitational settling term. Over sea
170 or ocean surfaces, the quasi-laminar boundary layer (QBL) may be disrupted by bursting bubbles,
171 resulting in an increase in downward movement of particles, which is parameterized by the approach
172 of Van den Berg et al. (2000), in which quasi-laminar resistance r_b is determined by Brownian
173 diffusion and impaction when QBL is intact, and by turbulence and washout velocity of particles by
174 spray drops when QBL is broken down. Below-cloud scavenging (BCS) of particles between cloud
175 base and ground surface represents capture processes of particle by falling hydrometeor through
176 Brownian and turbulent shear diffusion, interception and inertial impaction, and is parameterized by a
177 scavenging rate, which is a function of precipitation rate and collision efficiency of particle by
178 hydrometeor (Slinn, 1984).

179 A physically based scheme (namely A-G scheme) developed based on classical Köhler theory by
180 Abdul-Razzak and Ghan (1998, 2004) is incorporated into RIEMS-Chem to represent aerosol



181 activation into cloud droplet processes. This scheme calculates cloud droplet number concentration
182 (N_c) with not only aerosol number concentration, but also aerosol size distribution and composition,
183 updraft velocity and ambient supersaturation. Aerosols are activated if their critical supersaturation is
184 less than the maximum ambient supersaturation. The critical supersaturation for activating particles is
185 determined by curvature effect and solute effect. The maximum ambient supersaturation is calculated
186 by solving supersaturation balance equation (Abdul-Razzak and Ghan, 1998). The updraft velocity is
187 represented by the sum of grid mean updraft velocity and sub-grid updraft velocity, which is
188 diagnosed from vertical eddy diffusivity according to Ghan et al. (1997). The A-G scheme in
189 RIEMS-Chem has been applied over the western Pacific Ocean in spring 2014 and its prediction for
190 hourly CCN concentration at different supersaturations has been validated by cruise measurements
191 from the marginal seas of China to remote oceans southeast of Japan, which demonstrates a good
192 ability, with the correlation coefficient of 0.87 and normalized mean bias within 20%. More details on
193 the treatment and evaluation of marine aerosol activation refer to Han et al. (2019). Once N_c is
194 calculated by the A-G scheme, the cloud droplet effective radius r_e is calculated with the method of
195 Martin et al. (1994). The activated aerosols (into cloud droplet) are removed from the air. The auto
196 conversion rate from cloud water to rainwater is parameterized by the scheme of Beheng (1994),
197 which depends on N_c diagnosed and cloud liquid water content. The effect of aerosols on ice nuclei
198 and convective cloud is not treated in this model due to limited knowledge at present.

199

200 2.2 Aerosol physical and chemical properties

201 Ten aerosol types are simulated in RIEMS-Chem, which are sulfate (SO_4^{2-}), nitrate (NO_3^-),
202 ammonium (NH_4^+), black carbon (BC), primary organic aerosol (POA), secondary organic aerosol
203 (SOA), anthropogenic primary PMs ($\text{PM}_{2.5}$ and PM_{10}), dust, and sea salt.

204 Based on the observational analysis of aerosol mixing state in eastern China (Ma et al., 2017; Wu
205 et al., 2017), an internal mixing assumption is adopted for anthropogenic aerosols and they are
206 externally mixed with natural aerosols. The geometric mean radius and standard deviation of the
207 anthropogenic internal mixture are estimated to be $0.11 \mu\text{m}$ and 1.65, respectively, based on field
208 measurements (Ma et al., 2017). Mineral dust and sea salt are represented by 5 size bins ($0.1\sim 1.0$,
209 $1.0\sim 2.0$, $2.0\sim 4.0$, $4.0\sim 8.0$ and $8.0\sim 20.0 \mu\text{m}$). Feng et al. (2017) indicated that the measured total
210 organic carbon (TOC) in the western Pacific Ocean during the same period as this study was enriched



211 in $<0.3 \mu\text{m}$ (volume median diameter), which was mainly contributed by MPOA and the super-micron
212 TOC was generally below the detection limit. Accordingly, the geometric mean diameter of marine
213 organic aerosol number concentration was set to be $0.1 \mu\text{m}$, with a standard deviation of 1.6. The
214 number concentration is calculated by mass concentration as the formula in Curci et al. (2015). MPOA
215 can be mixed with sea salt both externally or internally. It is more likely to be externally mixed with
216 sea salt for finer aerosols ($<200 \text{ nm}$ in diameter) (Gantt and Meskhidze, 2013) and the effect of
217 externally mixed MPOA was found to be much more important than that of internally mixed MPOA
218 (Gantt et al., 2012b). So an external mixture of MPOA and sea salt is assumed in this study, this
219 means additional marine organic aerosols are produced to affect cloud properties and represents an
220 upper limit of indirect effect. There is little information on physical and chemical properties of marine
221 organic aerosols, some key parameters for calculation of aerosol activation, i.e. the number of ions the
222 salt dissociates into water, the osmotic coefficient, the mass fraction of soluble material, the density,
223 and molecular weight are set to be 3.0, 1, 0.1, 1.5 g m^{-3} , and 90, respectively, according to a few
224 previous studies (Abdul-Razzak and Ghan, 2004; Roelofs, 2008). The soluble mass fraction of MPOA
225 is assumed to be 0.2, slightly higher than that of MPOA (Liu and Wang, 2010; Westervelt et al., 2012).
226 An OM/OC ratio of 1.4 was applied to convert organic matter (OM) to OC (Gantt and Meskhidze,
227 2013).

228 The hygroscopic growth of aerosol is parameterized by a κ parameterization (Petters and
229 Kreidenweis, 2007). The hygroscopicity parameters (κ) for inorganic aerosol components, BC, POA,
230 SOA, dust, and sea salt are set to be 0.65, 0, 0.1, 0.2, 0.01 and 0.98, respectively (Riemer et al., 2010;
231 Liu et al., 2010; Westervelt et al., 2012). The hygroscopicity for MPOA and MPOA are assumed to be
232 the same as those for anthropogenic POA and SOA. Because there was limited information on the
233 optical properties of marine organic aerosols, the refractive index of anthropogenic POA and SOA was
234 used instead. The aerosol refractive index and hygroscopicity (κ) of the internally mixed aerosol are
235 calculated by volume-weighting of the parameters for each aerosol component. Aerosol optical
236 parameters including extinction coefficient, single scattering albedo, and asymmetry factor are
237 calculated by a Mie-theory based method developed by Ghan and Zaveri (2007), in which the aerosol
238 optical parameters are pre-calculated by the Mie theory and then fitted by Chebyshev polynomials
239 with a table of polynomial coefficients for looking up for aerosols with certain size and refractive
240 index. More detailed description refers to Li et al. (2020). This approach is much faster than



241 traditional Mie code with a similar level of accuracy and has been successfully used in estimating
242 aerosol optical properties over East Asia (Han et al. 2011).

243

244 2.3 Anthropogenic and natural emissions

245 Monthly mean anthropogenic emissions of sulfur dioxide (SO₂), nitrogen (NO_x), ammonia (NH₃),
246 non-methane volatile organic compounds (NMVOC), carbon monoxide (CO), BC, POA, and other
247 anthropogenic primary PM_{2.5} and PM₁₀ in China for the year 2014 are obtained from the MEIC
248 inventory (Multi-resolution Emission Inventory for China) which was developed by Tsinghua
249 University (<http://meicmodel.org>, last access: 2020/01/20). Anthropogenic emissions outside China
250 are taken from the MIX inventory which was developed to support the Model Inter-Comparison Study
251 for Asia phase III (MICS-Asia III) and the Hemispheric Transport of Air Pollution (HTAP) projects
252 (Li M. et al., 2017). Both inventories of MEIC and MIX have the same resolution of 0.5 degree. Open
253 biomass burning emissions of aerosols and gas precursors for the year 2014 with a spatial resolution
254 of 0.5 degree are derived from the Global Fire Emissions Database, Version 4.0 (GFED4) on a daily
255 basis (Giglio et al., 2013). The biogenic VOC emission is derived from the CAMS-BIO Global
256 biogenic emissions dataset (CAMS-GLOB-BIO v3.1) (Granier et al., 2019; Sindelarova et al., 2014)
257 distributed by ECCAD-GEIA (<https://permalink.aeris-data.fr/CAMS-GLOB-BIO>, last access:
258 2020/02/10) and the monthly mean biogenic emission for the year 2014 with a horizontal resolution of
259 0.25° is used. All the above emission data are bilinearly interpolated to the lambert projection of
260 RIEMS-Chem. The deflation of mineral dust is represented by the scheme of Han et al. (2004), which
261 is calculated online with RIEMS predicted meteorology.

262 The generation of sea salt aerosol through bubbles is represented by Gong (2003) which is
263 developed for sea salt radius from 0.07μm to 20μm based on the scheme of Monahan et al. (1986) and
264 it is modified by considering the influences of sea surface temperature (SST) (Jaeglé et al., 2011) and
265 relative humidity (RH) (Zhang et al., 2005).

266 The size-resolved marine primary organic aerosol (MPOA) emission is parameterized based on
267 the method of Gantt et al. (2011; 2012a), in which the emission rate of MPOA is the product of sea
268 spray emission rate and organic matter fraction of sea spray aerosol, which is expressed as a function
269 of wind speed, surface seawater Chl-a concentration, and aerosol size. The Chl-a data used in this
270 study is the Level-3 daily mean Chl-a concentration (mg m⁻³) product with 9 km resolution retrieved



271 from the VIIRS (Visible infrared Imaging Radiometer) sensor onboard the Suomi National
272 Polar-orbiting Partnership (SNPP) satellite platform (OBPG, 2018) (<http://oceandata.sci.gsfc.nasa.gov>,
273 last access: 2020/12/8). A brief description on this scheme with formulas is presented in the
274 supplement.

275 Marine isoprene emission released by phytoplankton activities is parameterized using the scheme
276 of Gantt et al. (2009) which considers light sensitivity of phytoplankton isoprene production and
277 dynamic euphotic depth (see more details in the supplement). Marine emission of monoterpene is
278 scaled by 0.2 to those of isoprene following the suggestion from Myriokefalitakis et al. (2010). The
279 marine abiotic source of isoprene (due to photochemical production in the sea surface microlayer)
280 may be important according to recent studies (Brüggemann et al., 2018; Conte et al., 2020). This
281 mechanism is not considered in this study because the production mechanism for marine abiotic
282 isoprene is poorly understood at present.

283

284 2.4 Model setup and experiment design

285 This study focused on the western Pacific Ocean of East Asia. The model domain covered most
286 areas of eastern China, the Korean Peninsula, Japan, parts of Southeast Asia, and a wide area of the
287 western Pacific Ocean (Figure 1). A Lambert conformal projection with 60 km horizontal resolution
288 was applied in the model. 16 vertical layers stretched unevenly from the surface to tropopause in a
289 terrain-following sigma coordinate with the first 8 layers within planetary boundary layer. The
290 simulation period was from 1 December 2013 to 31 December 2014 with the first month as model
291 spin-up and the whole year of 2014 was used for analysis. Final reanalysis data with $1^\circ \times 1^\circ$ resolution
292 and 6-hour interval from the National Centers for Environmental Prediction (NOAA/NCEP, 2000)
293 was used to provide initial and boundary conditions for meteorology. Chemical results derived from
294 the MOZART-4 (Model for Ozone and Related chemical Tracers, version 4; Emmons et al., 2010)
295 simulation with 6-hour interval were used to provide lateral conditions for trace gases and aerosols.
296 The full simulation (FULL) is designed by considering all anthropogenic and natural emissions,
297 including marine emissions of primary organic aerosol and sea salt, and a series of model simulations
298 are also conducted to estimate the direct and indirect radiative effect of MOA and their sensitivity to
299 MOA properties, which are described in the following sections.

300



301 2.5 Observations

302 In-situ measurements of PM₁₀, PM_{2.5}, and gas precursors (O₃, SO₂, and NO_x/NO₂) at coastal and
303 island sites in Japan and Republic of Korea were obtained from EANET (Acid Deposition Monitoring
304 Network in East Asia, <http://www.eanet.asia>, last access: 2020/01/23) (Figure 1). Hourly
305 concentrations of PM₁₀, SO₂, NO_x in Japan, NO₂ in Korea, and O₃ were automatically monitored at
306 six Japanese sites (Rishiri, Tappi, Sado-seki, Oki, Hedo, and Ogasawara) and three Korean sites (Jeju,
307 Kanghwa, and Imsil), whereas hourly PM_{2.5} concentrations were only available at three Japanese sites
308 (Rishiri, Sado-seki, and Oki). Sodium (Na⁺) concentrations sampled on a bi-weekly basis at the 6
309 coast/island EANET sites in Japan were also collected. Besides, hourly PM₁₀ and PM_{2.5}
310 concentrations monitored in the three coastal cities of China (Qingdao, Shanghai, and Fuzhou) were
311 also obtained from the CNEMC (China National Environmental Monitoring Center,
312 <http://www.cnemc.cn/>, last access: 2020/01/23) and used for model validation (Figure 1).

313 Carbonaceous aerosol (OC and BC) concentrations measured from two research cruise campaigns
314 covering the western Pacific during the spring and summer of 2014 (Figure 1) were collected and used
315 for model validation. The spring cruise campaign was carried out from 17 March to 22 April 2014
316 onboard the research vessel R/V Dongfanghong II, which started from Qingdao, sailed to the western
317 Pacific Ocean, and then returned (Figure 1) (Luo et al., 2016; Feng et al., 2017). OC and BC samples
318 were collected by an 11-stage MOUDI (Models110-IITM) (0.054–18 μm) equipped with
319 pre-combusted quartz filters onboard the vessel. Mass concentrations of total OC (primary and
320 secondary) and BC were determined by the thermal/optical carbon analyzer (Sunset Laboratory Inc.,
321 Forest Grove, OR). Totally 19 daily BC and OC samples were collected during the cruise. Detailed
322 information about this campaign and the sampling and analysis techniques were documented in Feng
323 et al (2017). The early summer campaign was carried out from 18 May to 12 June 2014 (Kang et al.,
324 2018). Total suspended particles (TSP) were collected on pre-combusted quartz filters using a
325 high-volume air sampler (Kimoto, Japan) onboard the KEXUE-1 Research Vessel during a National
326 Natural Science Foundation of China (NSFC) sharing cruise (Figure 1). This campaign covered low-
327 to mid-latitudes of the western Pacific Ocean (over the Yellow Sea and the East China Sea). Totally 51
328 half-day (daytime/nighttime) OC samples were obtained during this campaign. Detailed information
329 about this campaign and samples were described in Kang et al. (2018).

330 Besides the in-situ observations and cruise campaigns mentioned above, long-term observations



331 of OC and BC from previous publications were collected to help model comparison and analysis.
332 Carbonaceous aerosol samples (OC and BC) in TSP were continuously collected on a weekly basis
333 from 2001 to 2012 at Chichijima Island (the same place as Ogasawara in Figure 1), a remote island
334 located in the western North Pacific. The monthly mean OC and BC concentrations of the 12-year
335 average were reported by Boreddy et al. (2018) and used to verify the model performance over remote
336 oceans. Measurements of seasonal mean OC and BC concentrations in TSP at Huaniao Island (a
337 pristine island about 100 km southeast of Shanghai over the East China Sea, see Figure 1) from
338 October 2011 to August 2012 (Wang F. W. et al., 2015) and at Okinawa island (the same place as
339 Hedo in Figure 1) in the western Pacific Ocean from October 2009 to October 2010 (Kunwar and
340 Kawamura, 2014) were collected and used in this study. BC observations were conducted at Fukue
341 Island of western Japan using a continuous soot-monitoring system (COSMOS) (Figure 1) by Kanaya
342 et al. (2016) from 2009 to 2015.

343 Ground observations of AOD were obtained from the Aerosol Robotic Network (AERONET,
344 <https://aeronet.gsfc.nasa.gov/>, last access: 2020/06/03). Level 2 AOD observations for the year 2014
345 were collected at 7 coastal sites shown in Figure 1. Hourly and monthly mean observations were
346 derived from raw data and used for model comparison and statistics calculation. AOD at 550 nm was
347 used to match the model output. The level-3, daily deep blue global AOD product (in $1^{\circ} \times 1^{\circ}$ horizontal
348 resolution and at 550nm) retrieved by VIIRS sensor onboard the SNPP satellite platform (Sayer et al.
349 2018) were also collected to examine AOD spatial distribution.

350

351 3 Model validations

352 In this section, the model results for OC, BC, PM_{10} , $PM_{2.5}$, sodium concentrations, and AOD were
353 compared with a variety of observations from research cruise and monitoring networks to help
354 evaluate the model ability over wide areas from eastern China to the western Pacific Ocean. Because
355 the above comparison was for total OC mass concentration, we also compared the simulated SOA
356 from marine sources to cruise measured SOA tracer to examine the model performance for marine
357 organic aerosols.

358

359 3.1 Particulate matters (PM_{10} and $PM_{2.5}$), sodium (Na^+) and gas precursors

360 As particulate matter in remote marine atmosphere is mainly composed of sea salt, the model



361 performance for PM_{10} and $PM_{2.5}$ may partly reflect the model ability for sea salt simulation, which is
362 crucial to the estimation of MPOA emission.

363 Because the focus of this study is seasonal variation, the hourly PM_{10} and $PM_{2.5}$ observations and
364 corresponding simulations were averaged to be monthly means and shown in Figure 2. In general,
365 RIEMS-Chem performed quite well in simulating monthly variation of PM_{10} concentrations at both
366 the EANET sites (Figure 2a~2i) and CNEMC sites (Figure 2j~2l) for the year 2014, although model
367 biases still occurred at some sites, such as the underprediction in winter and spring in Jeju (Figure 2g)
368 and Imsil (Figure 2i) and the overprediction in May in Oki (Figure 2d) and Rishiri (Figure 2a). It was
369 striking that PM_{10} concentration peaked in May and was lowest in August at all Korean sites and
370 northern Japanese sites over northeast Asia (Figure 2a~2d and 2g~2i), which could be attributed to the
371 long-range transport of mineral dust from north China and Mongolia in spring and to the
372 southwesterlies consisting of mainly marine air masses in summer. It was noteworthy that the model
373 simulated seasonality and magnitude of PM_{10} agreed quite well with observations at the four island
374 sites of northern Japan (Rishiri, Tappi, Sado, and Oki) (Figure 2a~2d), where sea salt aerosol played a
375 more important role than those sites in Korea, implying sea salt concentrations could also be well
376 reproduced by the model. The seasonality of PM_{10} concentration at Hedo (Figure 2e) was different
377 from above, showing high values in winter as well besides the peaks in spring, which indicated
378 potential influence of continental anthropogenic sources under prevailing northwesterlies. The PM_{10}
379 level at Ogasawara (Figure 2f) was much lower than those at the other sites and its seasonality was
380 characterized by the minimum in summer ($5 \mu\text{g m}^{-3}$) and the maximum in spring. The model
381 reasonably reproduced the seasonality at Hedo (Figure 2e) and Ogasawara (Figure 2f) as well,
382 although it generally predicted lower values at Hedo and higher values at Ogasawara. As for PM_{10}
383 concentrations at the CNEMC sites of eastern China, the model simulated PM_{10} concentrations very
384 well for Shanghai (Figure 2k) and Fuzhou (Figure 2l) in terms of both monthly variation and
385 magnitude, showing higher values in spring and the maximum in winter in Shanghai, and an almost
386 stable level around $60 \mu\text{g m}^{-3}$ in Fuzhou throughout the year except for the elevated value in January.
387 The PM_{10} level in Qingdao (Figure 2j) was higher than those in Shanghai and Fuzhou, and reached the
388 maximum of $170 \mu\text{g m}^{-3}$ in January due to anthropogenic sources and the peak in March was resulted
389 from the effect of mineral dust.

390 The monthly variations of $PM_{2.5}$ concentrations at Rishiri, Sado, and Oki (Figure 2m~2o) were



391 similar to those of PM_{10} , but the peaks in May were not as evident as those of PM_{10} , because mineral
392 dust comprises a small fraction of fine particles and has less effect on $PM_{2.5}$ variation. The model
393 reproduced $PM_{2.5}$ concentrations very well at the three coastal sites of eastern China (Figure 2p~2r)
394 and the monthly variation of $PM_{2.5}$ concentrations resembled those of PM_{10} , because fine particle
395 accounts for a large fraction of PM mass in these Chinese megacities due to the dominant effect of
396 anthropogenic sources.

397 Table 1 shows that for all the 9 EANET sites, the overall mean PM_{10} concentration was $30.0 \mu g$
398 m^{-3} from observation and $28.5 \mu g m^{-3}$ from simulation, with the overall Pearson correlation coefficient
399 (R) of 0.65 (0.48~0.64) and the normalized mean bias (NMB) of -5% (-27~36%). For $PM_{2.5}$, the mean
400 concentrations averaged over the EANET sites were $10.9 \mu g m^{-3}$ from observation and $12.3 \mu g m^{-3}$
401 from simulation, with R and NMB of 0.61 (0.53~0.64) and 12% (0~21%), respectively. The annual
402 mean observed and simulated PM_{10} concentrations at the 3 CNEMC sites (Table 2) were $81.6 \mu g m^{-3}$
403 and $80.7 \mu g m^{-3}$, with R and NMBs of 0.65 (0.38~0.61) and -1% (-4~1%), respectively, while the
404 annual mean observed and simulated $PM_{2.5}$ concentrations, R, and NMB were $46.6 \mu g m^{-3}$, $43.4 \mu g$
405 m^{-3} , 0.70 (0.44~0.72), and -7% (-12~0%), respectively. The good performance statistics shown in
406 Table 1 and Table 2 suggest a good skill of RIEMS-Chem in reproducing PM levels from the coastal
407 regions of east China to the remote western Pacific. Figure 2, Table 1, and Table 2 also illustrate that
408 the spatial distribution of PM exhibited higher concentrations at the continental (costal) sites
409 (CNEMC sites, Jeju, Kanghwa, and Imsil) and lower concentrations at the remote island site
410 (Ogasawara) over the western Pacific, which were also reasonably reproduced by RIEMS-Chem.

411 Seasonal mean statistics of PM_{10} and $PM_{2.5}$ concentrations at the EANET and CNEMC sites were
412 also listed in Table 1 and Table 2. Statistics for spring (March-April-May, MAM), summer
413 (June-July-August, JJA), autumn (September-October-November, SON), and winter
414 (December-January-February, DJF) were calculated. PM_{10} observations generally exhibited higher
415 concentrations in MAM and DJF, moderate concentrations in SON, and lower concentrations in JJA at
416 most sites covering coastal areas (CNEMC sites, Jeju, Kanghwa, and Imsil) and remote islands (e.g.
417 Oki, Hedo, and Ogasawara). The model reproduced such seasonal variation of PM_{10} reasonably well
418 although some underestimations occurred from winter to spring at Jeju and Imsil (Figure 2g, 2i),
419 which could be attributed to the uncertainties in emissions (anthropogenic, biomass burning).

420 Comparison with observations of Sodium (Na^+) concentration at 6 Japan coastal/island sites from



421 EANET is conducted to further examine the model performance for sea salt. The modeled sodium is
422 estimated to be 38.56% of sea salt mass (Kelly et al., 2010), and the agreement between observation
423 and model simulation is generally satisfactory at all sites except at Oki in December, when the model
424 largely underpredict Na^+ . The model well reproduces the seasonality of sodium concentration, with
425 the maximum in winter and the minimum in summer (Figure 3). The model predicts sodium
426 concentration best at Ogasawara, with the correlation coefficient of 0.85 and NMB of 5%. The overall
427 correlation coefficient for all sites is 0.50, with NMB of -11% (Table S1).

428 In all, RIEMS-Chem was able to reasonably reproduce the spatial distribution and seasonal
429 variation of PM_{10} , $\text{PM}_{2.5}$, and sodium concentrations in the marine environment of the western Pacific.
430 The above good performances give us confidence in the estimation of marine sea salt emission.

431 In addition, the overall statistics were generally acceptable for gas precursors (O_3 , SO_2 , and
432 NO_x/NO_2), indicating atmospheric chemistry processes could be reasonably represented by the model
433 over the western Pacific. (see statistics in Table S2)

434

435 3.2 Carbonaceous aerosols

436 Modeled BC and OC concentrations were compared with observations from research cruises and
437 from previous publications at coastal/remote islands. BC is considered to be inert and chemical
438 inactive, so it is governed solely by physical processes and a good indicator of long-range transport.
439 The analysis of BC can help identify regions with large continental influence.

440

441 3.2.1 Comparison with research cruise measurements

442 Figure 4a shows the observed and simulated daily BC concentrations along the cruise track
443 during the spring campaign. An obvious spatial gradient was found for BC concentration, which was
444 characterized by apparent higher concentrations of $0.5\sim 4.2 \mu\text{g m}^{-3}$ over the marginal seas of China
445 (the Yellow Sea and East China Sea, 18~19 March and 21~22 April) and very low concentrations of
446 ~ 0 to $<0.2 \mu\text{g m}^{-3}$ over open oceans (during most of the measurement days). It is interesting to note
447 that an observed BC peak occurred on 21 March, which could be attributed to the long-range transport
448 of biomass burning plumes from northeast Asia (Luo et al., 2016; 2018). The model generally
449 reproduced the spatial and temporal variations of BC concentration during the campaign period;
450 however, the BC peak on 21 March was missed by the model simulation. Uncertainties in biomass



451 burning emission could be responsible for such model bias. On average, the measured and simulated
452 BC concentrations during this campaign onboard the Dongfanghong II cruise were $0.49 \mu\text{g m}^{-3}$ and
453 $0.55 \mu\text{g m}^{-3}$, respectively, with the R and NMB of 0.87 and 13% (Table 3).

454 Figure 4b shows the daily mean OC concentrations from observation and model simulation for
455 the same cruise. In general, the observed OC exhibited a similar spatial distribution and temporal
456 variation to that of BC, with higher concentrations over the marginal seas and relatively lower
457 concentrations over open oceans. The model generally captured the spatial-temporal features along the
458 cruise track. Like BC, the observed OC concentrations were high on 21 and 25~26 March mainly due
459 to the continental outflow of biomass burning emissions from northeast Asia, and the model largely
460 underpredict the high OC observation in these days. It is noteworthy that two OC peaks appeared on
461 10 and 12 April when the ship was over the open ocean east of Japan (the ship location was around
462 33.5°N , 146.0°E on 10 April and around 36.5°N , 145.0°E on 12 April, approximately 400~500 km to
463 the east of Japan), whereas the elevation of BC concentration was not evident. Because BC and OC
464 are often originated from the same anthropogenic and biomass sources, the inconsistency in daily
465 variation between BC and OC in these areas implied a potential influence of marine sources rather
466 than that from anthropogenic and biomass burning emissions. Coincidentally, during these days, daily
467 Chl-a concentrations over the oceanic areas east of Japan (the region of 35°N to 43°N and 140.0°E to
468 150.0°E , north to the ship location) reached as high as 45 mg m^{-3} , as a comparison, the monthly mean
469 Chl-a concentration in April over the same region was in a range of 2 to 14 mg m^{-3} . The apparent
470 higher Chl-a concentration during these days could induce changes in marine primary organic
471 emissions. On 10 April, the wind direction in the vicinity of the cruise was mainly southwesterly,
472 backward trajectory (figure not shown) indicates that air parcels travelled over low Chl-A regions to
473 the southwest of the cruise, implying a small effect of MOA. On this day, the fraction of land-OC (OC
474 originated from continental sources) in total OC was 68%, which was larger than that of marine
475 organic carbon (marine-OC) (32%) as shown in Figure 4b. On 12 April, northwesterly winds prevailed
476 over the cruise region, with backward air trajectory traveling over strong Chl-A regions to the
477 northeast of Japan (figure not shown), marine-OC aerosols produced from the bloom regions could be
478 blown to the southeast where ship located, leading to the elevation of OC concentrations (Figure 4b).
479 Marine-OC (percentage contribution of 74%) dominated over land-OC (26%) in the total OC
480 concentration on this day. The model improves OC simulation on 10 and 12 April when considering



481 marine organic aerosols (marine-OC in Figure 4b). The cruise campaign average OC concentration
482 was $1.20 \mu\text{g m}^{-3}$ from observation and $1.14 \mu\text{g m}^{-3}$ from simulation, with the R and NMB of 0.66 and
483 -5%, respectively (Table 3). The inclusion of marine-OC (including both primary and secondary OC)
484 reduced the model bias from -33% to -5% along the cruise. The average contribution of marine-OC to
485 the total OC mass in the marine atmosphere was approximately 29% along the cruise, with lower
486 contributions of 11~27% over the marginal seas of China (18~19 March and 21~22 April) and higher
487 contributions of 32~74% over the open oceans (5~18 April) (Figure 4b), demonstrating an increasing
488 importance of marine organic aerosols to total OC mass from the marginal seas to remote open
489 oceans.

490 Shown in Figure 4c is OC samples collected onboard the KEXUE-1 Research Vessel over the
491 East China Sea during the early summer campaign and the corresponding model results along the
492 cruise track. There were four OC peaks observed during the campaign, with three occurring over the
493 northern parts of the East China Sea (on 20 May, 26~29 May, and 1~5 June) and one over the southern
494 part of the East China Sea on 22 May. The model reproduced the OC variation quite well during most
495 of the cruise track, capturing the three OC peaks over the northern parts of the East China Sea
496 although low biases occurred for the first peak (over the area of 27.5°N to 30.0°N and 121.6°E to
497 121.9°E). The model missed the second OC peak on 22 May over the southern part of the East China
498 Sea (over the area of 22°N to 23°N and 121.5°E to 122.2°E). Kang et al. (2018) proposed that this
499 peak was seriously affected by biogenic and biomass burning emissions from Southeast Asia
500 (Philippines) because the OC concentrations from 21 to 25 May were characterized by high
501 abundance of sesquiterpene-derived SOA which was mainly originated from terrestrial photosynthetic
502 vegetation (e.g. trees and plants). Uncertainties in emission inventories, such as missing some
503 biogenic sources (e.g. fungal spores, Fröhlich-Nowoisky et al. 2016) could be partly responsible to the
504 model biases. In addition, some regions of Southeast Asia (e.g. Philippines) were not included in the
505 study domain, instead, their influence on the study domain was represented by chemical boundary
506 conditions from MOZART simulation, so, the uncertainties in chemical boundary conditions may also
507 contributed to such biases. At the time of the third (25°N to 26°N and 118.8°E to 121.7°E) and fourth
508 (28°N to 28.7°N and 119.6°E to 122.7°E) OC peaks, the ship was close to the shore and
509 predominately affected by continental sources (such as anthropogenic and biomass burning emissions),
510 the model captured the peaks quite well in terms of both temporal variation and magnitude. On



511 average, the observed and simulated OC concentrations from the KEXUE-1 cruise were $4.26 \mu\text{g m}^{-3}$
512 and $3.68 \mu\text{g m}^{-3}$, respectively, with R and NMB of 0.75 and -13% (Table 3). The inclusion of
513 marine-OC reduced the NMB from -19% to -13%. Along the cruise track, marine-OC was estimated
514 to account for 6% (1~60%) of the total OC mass on average, with lower contribution over the seas
515 close to the continent (1~9%) and higher contribution over the seas far from the continent (7~60%).
516 During the KEXUE-1 cruise campaign, the contribution of marine-OC to total OC mass was
517 obviously lower than that during the spring campaign conducted by the Dongfanghong II, because this
518 cruise over the marginal seas of China was more affected by continental outflow of anthropogenic and
519 biomass emissions compared with that mainly over the open oceans.

520

521 3.2.2 Comparison with measurements at island and coastal sites

522 Figure S1 shows the modeled BC is generally consistent with observations at island sites
523 (Huaniao, Fukue, Okinawa, Chichijima) in terms of both spatial distribution and seasonal variation,
524 indicating a good skill of RIEMS-Chem in representing the physical processes and long-rang transport
525 of carbonaceous aerosols over the western Pacific.

526 OC observations are limited in the western Pacific Ocean. We collected observations at islands
527 from previous publications (Boreddy et al., 2018; Kunwar and Kawamura, 2014; Wang F. W. et al.,
528 2015) for model comparison. Figure 5 shows the model simulated and observed seasonal/monthly
529 mean OC concentrations at the three islands. It should be kept in mind that the observations are
530 averages of different years. At Huaniao Island (Figure 5a), a distinct seasonality of OC observation
531 was shown, with the highest OC concentration of $4.7 \mu\text{g m}^{-3}$ in DJF, followed by $3.7 \mu\text{g m}^{-3}$ in MAM
532 and $3.8 \mu\text{g m}^{-3}$ in SON, and the minimum of $1.1 \mu\text{g m}^{-3}$ in JJA (Table 4). It was encouraging that
533 RIEMS-Chem reproduced the OC seasonality at Huaniao Island quite well (Figure 5a), despite the
534 different years between simulation and observation. The simulated OC was also divided into land-OC
535 and marine-OC to quantify the relative contribution of these sources to total OC mass. The simulated
536 annual mean OC concentration was $3.2 \mu\text{g m}^{-3}$, in which $2.6 \mu\text{g m}^{-3}$ (81%) was contributed by
537 land-OC and $0.6 \mu\text{g m}^{-3}$ (19%) by marine-OC (Table 4). The simulation was very close to the
538 observation of $3.3 \mu\text{g m}^{-3}$ (Table 4). It was striking that the inclusion of marine-OC obviously
539 improved the model performance, reducing the NMB from -21% to -3%, although the improvement of
540 prediction for SOA from land source may also reduce the model bias at Huaniao island. It was



541 noteworthy that marine-OC exhibited the maximum value in MAM and the minimum value in JJA.
542 The higher Chl-a concentration over the East China Sea in MAM might be responsible for the
543 maximum at Huaniao Island (Figure 7h and Table 7), whereas the lowest sea salt emission flux could
544 result in the minimum in summer (Table 7). In terms of seasonal mean, marine-OC accounted for 12%,
545 22%, 19%, and 23% of the total OC concentration in DJF, MAM, JJA, and SON, respectively, with an
546 annual mean contribution of 19% at Huaniao Island. The lowest relative contribution (12%) of
547 marine-OC in winter was attributed to the maximum anthropogenic OC emissions in eastern China in
548 this season.

549 At Okinawa (Figure 5b), the observed total OC showed the maximum in MAM, followed by that
550 in JJA, and the lower ones in DJF and SON during October 2009-2010. Figures 5a and 5b also show
551 that the seasonal cycling of OC concentration at Okinawa (Figure 5b) differed a lot from that at
552 Huaniao Island (Figure 5a). The high OC concentration in summer at Okinawa could be attributed to
553 higher SOA produced by local biogenic VOC emissions (Kunwar and Kawamura, 2014). The model
554 generally reproduced the seasonal variation of OC except that it predicted lower OC level in summer,
555 which could be due to the exclusion of local biogenic VOC emissions in the CAMS-GLOB-BIO
556 emission inventory. In terms of annual average, the observed OC concentration was $1.8 \mu\text{g m}^{-3}$, larger
557 than the simulations of $1.3 \mu\text{g m}^{-3}$ from the FULL case including marine-OC and of $1.1 \mu\text{g m}^{-3}$ from
558 the case excluding marine organic emissions (Table 4). The inclusion of marine organic emissions
559 improved OC simulation at Okinawa, reducing the NMB from -39% to -28%. It was estimated that
560 marine-OC accounted for 18%, 17%, 10%, and 18% of total OC mass concentration at Okinawa in
561 DJF, MAM, JJA, and SON, respectively, with an annual mean contribution of 17%. The relatively
562 smaller contribution of marine-OC to the total OC mass at Okinawa than that at Huaniao Island (19%)
563 could be attributed to the higher Chl-a concentration and MPOA emission flux in the marginal seas of
564 China than those over remote western Pacific south of Japan (Figure 7).

565 Long-term average (2001-2012) of monthly mean OC concentrations at Chichijima Island
566 reported by Boreddy et al. (2018) and the simulated monthly mean OC concentration in 2014 were
567 shown in Figure 5c. The observations show higher OC levels from January to March mainly due to
568 continental outflows. It was noticed that the simulated OC levels in April-May were apparently higher
569 than observations, which could be associated with different time periods between observation and
570 simulation, and with potentially stronger continental outflows and bloom in spring 2014 than those of



571 ten-year averages. OC observations were relatively lower in summer and autumn due to the
572 dominance of high-pressure system and pristine ocean air mass over the western Pacific (Figure 9d
573 and 9e). The model tended to predict lower OC level in summer and autumn (Figure 5c). Boreddy et
574 al. (2018) indicated that in summer and autumn, OC at Chichijima was often influenced by long-range
575 transport of biomass burning plumes from Southeast Asia, which was not well represented in the
576 model (using chemical boundary conditions from MOZART-4 instead) and led to low model bias. On
577 average, the annual mean OC concentration was $0.76 \mu\text{g m}^{-3}$ from observation, and $0.78 \mu\text{g m}^{-3}$ from
578 the FULL case, and $0.65 \mu\text{g m}^{-3}$ without considering marine-OC (Table 5). The inclusion of marine
579 organic emissions reduced the annual mean NMB from -13% to 3% and enhanced the correlation
580 coefficient from 0.56 to 0.6 at this site. The apparent better simulation from the FULL case indicated
581 the necessity of inclusion of marine organic emissions for simulating OC over the remote oceans of
582 the western Pacific. Both observation and model simulation revealed higher seasonal mean OC
583 concentrations in MAM (observed: $0.83 \mu\text{g m}^{-3}$, simulated: $0.91 \mu\text{g m}^{-3}$) and DJF (observed: $0.90 \mu\text{g m}^{-3}$
584 m^{-3} , simulated: $1.2 \mu\text{g m}^{-3}$) when the measurement site was frequently influenced by continental
585 outflows, whereas lower concentrations in JJA (observed: $0.65 \mu\text{g m}^{-3}$, simulated: $0.47 \mu\text{g m}^{-3}$) and
586 SON (observed: $0.66 \mu\text{g m}^{-3}$, simulated: $0.57 \mu\text{g m}^{-3}$) when clean maritime air masses or biomass
587 burning plumes from Southeast Asia (e.g. Philippine) influenced this region. The highest marine-OC
588 concentration was $0.19 \mu\text{g m}^{-3}$ in MAM, followed by $0.16 \mu\text{g m}^{-3}$ in DJF and $0.11 \mu\text{g m}^{-3}$ in SON, and
589 the lowest one of $0.05 \mu\text{g m}^{-3}$ in JJA. However, the percentage contribution of marine-OC to the total
590 OC mass was estimated to be largest in SON (20%), followed by 18% in DJF, 16% in MAM, and
591 lowest in JJA (10%), with an annual mean contribution of 16% (Table 5). The largest contribution in
592 SON was associated with the relatively lower total OC concentration as shown in Figure 5c. The
593 relative contribution from marine-OC to total OC at Chichijima Island resembled that at Okinawa in
594 terms of annual and season averages.

595 The above comparison against a variety of OC observations demonstrated a generally good skill
596 of RIEMS-Chem in simulating OC over the western Pacific in terms of seasonal variation and
597 magnitude. The model results from the FULL case indicated that including marine organic emissions
598 improved OC simulation over the western Pacific Ocean.

599

600 3.2.3 SOA over the western Pacific



601 Recently, Guo et al. (2020) reported SOA observations in the marine atmosphere from the
602 marginal seas of east China to the northwest Pacific Ocean. The measurements were conducted on
603 three research cruises in the spring and early summer of 2014 and in the spring of 2017. Total
604 suspended particulate (TSP) samples were collected from 19 March to 21 April 2014 over the
605 northwestern Pacific Ocean (NWPO), from 30 April to 17 May 2014 over the Yellow and Bohai seas
606 (YBS), and from 29 March to 4 May 2017 over the South China Sea (SCS). SOA concentration was
607 derived by using a tracer-based method. The measured SOA concentrations were 467 ng m^{-3} over the
608 YBS, 617 ng m^{-3} over the SCS, and 155 ng m^{-3} over the NWPO, respectively. The model simulated
609 period and regional mean SOA concentrations were 664 ng m^{-3} over the YBS, 466 ng m^{-3} over the
610 SCS, and 157 ng m^{-3} over the NWPO, which were generally consistent with the above observations,
611 although the study periods are not exactly the same. Guo et al. (2020) also presents the tracer-based
612 estimations of isoprene and monoterpene derived SOA in the air masses from ocean (assuming marine
613 sources), which were 1.7 ng m^{-3} and 0.3 ng m^{-3} , respectively, over the western Pacific to the southeast
614 of Japan, whereas the modeled SOA concentrations produced from marine isoprene and monoterpene
615 emissions along the cruise track were 1.55 ng m^{-3} and 0.28 ng m^{-3} , respectively, generally agreeing
616 with the tracer-estimation. However, it should be mentioned that there could be uncertainties in such
617 comparison. First, the isoprene- and monoterpene-derived SOA tracers in the air masses categorized
618 as marine sources by Guo et al (2020) might include SOA tracers from terrestrial isoprene and
619 monoterpene under the prevailing northwesterly winds in spring, which could bias the estimation high;
620 second, the measured tracer could just comprise a part of total SOA tracers, which might bias the
621 estimation low. Despite these uncertainties, the cruise measured SOA concentration derived from
622 marine isoprene and monoterpene was approximately several ng m^{-3} over the western Pacific, and it
623 can reach approximately 10 ng m^{-3} even through dividing by a mass fraction of tracer compound to
624 yield the concentration of total SOA tracers. It was noteworthy that both observation and model
625 simulation exhibited a decreasing SOA concentration from marginal seas of China to remote oceanic
626 areas. In all, the model reproduced the SOA levels in the marine atmosphere of the western Pacific
627 Ocean reasonably well.

628 The comparison of the magnitudes between SOA and OA mass (1.4 times OC mass)
629 concentrations shown above indicates that SOA concentration was approximately 1~2 orders of
630 magnitude lower than OA over the western Pacific. Previous observation studies using the



631 tracer-based approach also indicated that the percentage contribution of SOA to OA was quite low
632 over some marine areas (Fu et al., 2011; Hu et al., 2013; Bikkina et al., 2014; Zhu et al., 2016). For
633 example, at Okinawa island, even considering all biogenic sources (including isoprene, monoterpene,
634 and sesquiterpene of both terrestrial and oceanic origins), the measured concentration of total
635 biogenic-SOA tracers was still less than 100 ng m^{-3} , with majority of SOA tracers from local terrestrial
636 biogenic emissions (Zhu et al., 2016). The above studies suggested that primary organic aerosols were
637 more important in remote marine atmosphere.

638

639 3.3 Aerosol optical depth

640 Figure 6 shows the temporal variations of the observed and simulated monthly mean AOD at the
641 7 AERONET sites. In general, RIEMS-Chem simulated the monthly mean AOD reasonably well in
642 terms of magnitude and monthly variation at almost all sites, although some biases occurred during
643 some months, such as the overpredictions in August at Fukuoka and in April at EPA-NCU, and the
644 underprediction in July at Yonsei University. For the sites in the northern oceanic areas (Ussuriysk,
645 Yonsei_University, Gwangju_GIST, and Fukuoka, Figure 6a~6d), both observations and simulations
646 generally exhibited higher AOD values in summer (JJA), moderately high AOD values from late
647 winter (JF) to spring (MAM), and relatively lower AOD values in autumn (SON). The simulated
648 higher inorganic aerosol concentrations in summer and late spring months could be responsible for the
649 higher AOD values in these regions. Besides, the higher relative humidity in summer due to the
650 predominant influence of maritime air masses also contributed to the maximum AOD values during
651 summer months (JJA) at these sites. On the other hand, for the sites in the southern oceanic areas
652 (EPA-NCU and Chen-Kung_Univ, Figure 6e and 6f), the monthly mean AOD was apparently higher
653 from March to April and remained low levels during the rest months. The above AOD peaks in spring
654 could be attributed to the continental outflows of biomass burning plumes originated from Southeast
655 Asia, which were most active in springtime in those regions (Hsiao et al., 2017; Tao et al., 2020).
656 Table 6 shows the performance statistics for hourly AOD at these AERONET sites. The overall annual
657 mean AOD for the 7 sites was 0.34 from model simulation, which was very close to the observation of
658 0.36, with the NMB of -6% and the overall correlation coefficient of 0.54 (0.40~0.67). The statistics
659 indicate that the model was able to reproduce aerosol optical properties over the coastal regions and
660 islands around the western Pacific Ocean.



661 The model simulated annual mean AOD at 550 nm are also compared with the VIIRS retrievals
662 (Figure S2), which indicates the model is generally capable of reproducing AOD distribution and
663 magnitude in the study domain. The generally high model bias over the western Pacific could be
664 attributed to potential overpredictions of inorganic aerosol concentration and relative humidity. AOD
665 reflects the column integrated extinction coefficient due to all aerosols.

666 At the AERONET sites, the model simulated annual mean percentage contribution of MOA to
667 AOD varied from 1.4% to 3.2% with an overall average of 1.9%. For the oceanic VIIRS region, the
668 mean contribution of MOA to AOD was approximately 2%.

669

670 4 Model results

671 4.1 Marine primary organic and isoprene emissions

672 Figure 7 shows the estimated annual and seasonal mean MPOA emission rates over the western
673 Pacific of East Asia. The MPOA emission mainly occurred over two hotspot regions: the marginal
674 seas of China including the East China Sea, the Yellow Sea, and the Bohai Sea (EYB, denoted in
675 Figure 7a) and the northern parts of the western Pacific northeast of Japan (NWP, denoted in Figure
676 7a), with annual mean emission rates varying from $0.9 \times 10^{-2} \mu\text{g m}^{-2} \text{ s}^{-1}$ to $1.8 \times 10^{-2} \mu\text{g m}^{-2} \text{ s}^{-1}$. In SON,
677 high MPOA emission occurred in both the EYB and NWP regions, with the maximum up to 3.5×10^{-2}
678 $\mu\text{g m}^{-2} \text{ s}^{-1}$ in the NWP (Figure 7e), whereas MPOA emission was very low over the EYB in JJA
679 (Figure 7d). The maximum seasonal mean emission rate of MPOA approached $3.6 \times 10^{-2} \mu\text{g m}^{-2} \text{ s}^{-1}$
680 over the Yellow Sea in DJF (Figure 7b), which was approximately 1/10 of the annual mean
681 anthropogenic POA emission rate in north China (on the order of $1.0\text{--}3.0 \times 10^{-1} \mu\text{g m}^{-2} \text{ s}^{-1}$). Table 7
682 presents the seasonal and annual averages of MPOA emission averaged over the western Pacific and
683 the EYB and NWP regions. In terms of oceanic average of the western Pacific, the mean MPOA
684 emission generally exhibited the largest emission rate in SON ($0.20 \times 10^{-2} \mu\text{g m}^{-3} \text{ s}^{-1}$), moderately high
685 emission rates in DJF ($0.18 \times 10^{-2} \mu\text{g m}^{-2} \text{ s}^{-1}$) and MAM ($0.17 \times 10^{-2} \mu\text{g m}^{-2} \text{ s}^{-1}$), and the lowest one in
686 JJA ($0.08 \times 10^{-2} \mu\text{g m}^{-2} \text{ s}^{-1}$), with an annual average of $0.16 \times 10^{-2} \mu\text{g m}^{-2} \text{ s}^{-1}$ (Table 7). It is interesting to
687 note that the seasonal variation of MPOA emission was not consistent with that of Chl-a concentration,
688 which exhibited higher values in SON and JJA and the lowest one in DJF (Table 7). This is because
689 MPOA emission rate is determined by the combined effect of Chl-a concentration and sea salt
690 emission flux, and sea salt flux is mainly controlled by surface wind speed according to the scheme of



691 Gong (2003). In terms of seasonal and domain average over the western Pacific, the maximum Chl-a
692 concentration and the second largest sea salt emission flux in SON led to the largest MPOA emission
693 in autumn (Table 7). However, although Chl-a concentration was also high in JJA (1.07 mg m^{-3} , Table
694 7), the sea salt flux was minimum in JJA ($0.14 \text{ } \mu\text{g m}^{-2} \text{ s}^{-1}$, Table 7) due to the weakest wind speed (3.0
695 m s^{-1} , Table 9), resulting in the lowest MPOA emission in summer (Table 7). Although the sea salt
696 emission flux reached the maximum in DJF (Table 7) due to the largest wind speed in this season
697 (Table 9), the winter Chl-a concentration was lowest, leading to a moderate MPOA emission in winter
698 (Table 7), in a similar magnitude to that in spring when moderately high Chl-a concentration and
699 relatively low sea salt flux occurred. In all, the MPOA emission rate over the western Pacific exhibited
700 an apparent seasonality of $\text{SON} > \text{DJF} \approx \text{MAM} > \text{JJA}$.

701 For the EYB region, the maximum MPOA emission occurred in winter (DJF) (Figure 7b and
702 Table 7) with a seasonal and domain average of $1.2 \times 10^{-2} \text{ } \mu\text{g m}^{-2} \text{ s}^{-1}$, which was 10 times larger than
703 the minimum of $0.12 \times 10^{-2} \text{ } \mu\text{g m}^{-2} \text{ s}^{-1}$ in summer (JJA) (Figure 7d and Table 7). Although Chl-a
704 concentrations were similar between DJF and JJA, the sea salt flux in DJF was approximately 9 times
705 that in JJA (Table 7). So, the seasonality of MPOA emission in the EYB region was mainly
706 determined by that of sea salt emission flux due to the weak seasonal variation of Chl-a concentration.
707 Differently, in the NWP region, MPOA emission exhibited the maximum value in SON, followed by
708 those in MAM and DJF, and the lowest ones in JJA (Table 7). It is interesting to note that although
709 both the Chl-a concentration and sea salt emission flux were slightly higher in MAM than those in
710 SON, the MPOA emission (related to both Chl-a concentration and sea salt emission) was higher in
711 SON, which could be due to the slight negative correlation between Chl-a concentration and sea salt emission in MAM, but
712 the slight positive one in SON. The MPOA emissions in winter and summer were in a similar level in
713 the NWP region, about 40% lower than that in autumn.

714 The distribution pattern of MPOA emission in the western Pacific from this study is similar to
715 those from previous model studies (Spracklen et al., 2008; Gantt et al., 2009; Huang et al., 2018), but
716 the magnitude of the simulated MPOA emission flux is larger than previous estimates. For example,
717 the annual mean MPOA emission rates over the western Pacific were estimated to vary from 0.1 to
718 approximately $12 \text{ ng m}^{-2} \text{ s}^{-1}$ in previous studies (Spracklen et al., 2008; Vignati et al., 2010; Gantt et
719 al., 2011; Long et al., 2011; Huang et al., 2018), whereas the estimates in this study ranged from 3 to
720 $18 \text{ ng m}^{-2} \text{ s}^{-1}$ (Figure 7a). The larger marine POA emission estimated in this study could be attributed



721 to the application of the daily mean Chl-a concentration from satellite retrievals and of a finer model
722 grid resolution (60 km) compared with those in global models. On average, the annual MPOA
723 emission was estimated to be 0.78 Tg yr^{-1} over the western Pacific (with an ocean area of 1.58×10^7
724 km^2) from this study. The regions of EYB and NWP comprised approximately 2% and 18% of the
725 western Pacific in terms of area, respectively, but they contributed 8% and 46% of the MPOA annual
726 emission (Tg yr^{-1}). This study revealed that the EYB and NWP are important bloom regions,
727 accounting for more than half of the total MPOA emission over the western Pacific.

728 Table S3 presents the simulated marine isoprene emission fluxes in comparison with
729 observation-based estimates over the western Pacific of East Asia and other oceans from previous
730 studies. Over the western North Pacific, the observed marine isoprene emission flux showed larger
731 values in May ($140\text{--}143.8 \text{ nmol m}^{-2} \text{ day}^{-1}$), a moderate value in August ($\sim 55.6 \text{ nmol m}^{-2} \text{ day}^{-1}$), and
732 the lowest one in winter ($\sim 21.4 \text{ nmol m}^{-2} \text{ day}^{-1}$). The model simulation generally agreed with
733 observation in terms of both seasonality and magnitude except for the low bias in spring ($85\text{--}89 \text{ nmol}$
734 $\text{m}^{-2} \text{ day}^{-1}$ in spring, $\sim 63 \text{ nmol m}^{-2} \text{ day}^{-1}$ in summer, and $\sim 26 \text{ nmol m}^{-2} \text{ day}^{-1}$ in winter), which could be
735 associated with the different years. According to equations (2) and (3), both Chl-a concentration and
736 incoming solar radiation determine marine biogenic VOCs emission, the larger isoprene flux in May
737 was mainly due to the maximum Chl-a concentration in spring over the NWP region (Table 7). Over
738 the marginal seas of China, Li J. L. et al. (2017; 2018) observed higher marine isoprene emission flux
739 in July-August ($\sim 161.5 \text{ nmol m}^{-2} \text{ day}^{-1}$) than those in October-November ($\sim 48.3 \text{ nmol m}^{-2} \text{ day}^{-1}$) and
740 May-June ($\sim 36.1 \text{ nmol m}^{-2} \text{ day}^{-1}$) during 2013-2014. The model well reproduced the seasonal trend
741 and magnitude of isoprene flux, with corresponding mean values of $130 \text{ nmol m}^{-2} \text{ day}^{-1}$, 48 nmol m^{-2}
742 day^{-1} , and $35 \text{ nmol m}^{-2} \text{ day}^{-1}$ during the same periods of 2014, respectively. The apparently higher
743 isoprene flux in July-August was mainly resulted from the strongest solar radiation in summer,
744 although the Chl-a concentration was not highest in this season in the EYB region (Table 7). Table S3
745 also lists previously observed marine isoprene emission fluxes over the Southern Ocean and Arctic
746 Ocean in summer for reference. The domain-wide annual marine isoprene emission estimated over the
747 western Pacific was 0.015 Tg yr^{-1} in this study. Arnold et al. (2009) calculated with GEOS-Chem
748 model a global-annual isoprene emission of 0.31 Tg yr^{-1} . However, some previous studies (Arnold et
749 al., 2009; Booge et al., 2016) found the emission flux calculated by current marine isoprene emission
750 schemes tended to yield lower isoprene concentration in marine atmospheres compared with



751 observations.

752

753 4.2 Marine organic aerosols and their relative importance

754 Annual and seasonal mean near surface MOA concentrations, MSOA concentrations, and the
755 percentage contributions of MOA to total OA mass in the study domain were shown in Figure 8. The
756 spatial distributions of MOA concentrations (Figure 8a~8e) generally resembled those of MPOA
757 emissions (Figure 7a~7e). It is remarkable that MPOA concentration (MOA minus MSOA) was
758 approximately 1~2 orders of magnitude higher than MSOA concentration (with concentration of
759 several ng m^{-3}) in the western Pacific (Figure 8a~8e vs Figure 8f~8j), indicating that MPOA
760 constituted a dominant fraction of MOA, which will be discussed below. Figure 8a shows that high
761 MOA concentrations mainly occurred over the EYB and NWP regions, with the annual and regional
762 averages being $0.48 \mu\text{g m}^{-3}$ and $0.59 \mu\text{g m}^{-3}$, respectively (Table 8), accounting for 13% (6~30%) and
763 42% (30~60%) of total OA mass in these two regions, respectively (Figure 8k and Table 8). The larger
764 MOA contribution over the NWP was attributed to the high MOA level and the relatively low total OA
765 level there. It is noticed that MOA even influenced the coastal areas of eastern China. The annual
766 mean MOA concentration decreased from approximately $0.5 \mu\text{g m}^{-3}$ in coastal areas to $0.1 \mu\text{g m}^{-3}$ in
767 the inland areas (Figure 8a), accounting for approximately 2% to 6% of the near-surface OA mass in
768 the coastal regions (Figure 8k). The maximum seasonal mean MOA concentration over the coastal
769 areas of eastern China could be up to $0.6 \mu\text{g m}^{-3}$ to $0.8 \mu\text{g m}^{-3}$ in MAM (Figure 8c) and SON (Figure
770 8e). The domain and seasonal mean MOA concentration over the western Pacific exhibited the
771 maximum value in MAM ($0.37 \mu\text{g m}^{-3}$), follow by that in SON ($0.26 \mu\text{g m}^{-3}$), and relatively lower
772 concentrations in JJA ($0.23 \mu\text{g m}^{-3}$) and DJF ($0.21 \mu\text{g m}^{-3}$) (Table 8). It was noteworthy that the
773 seasonality of MOA concentration was different from that of MPOA emission, which could be
774 attributed to the influence of different meteorological conditions and physical processes. In the
775 western Pacific, although MPOA emission peaked in SON (Table 7), MOA concentration peaked in
776 MAM (Table 8). It is noticed that precipitation was lowest and wind speed was low in MAM (Figure
777 9c and 9h, Table 9), leading to a smaller dry deposition velocity (Zhang et al. 2001) and the weakest
778 wet scavenging, both favored accumulation of MOA and thus resulted in the highest MOA level in
779 spring. On the contrary, due to the maximum wind speed and relatively more precipitation in DJF
780 (Figure 9b and 9g, Table 9), the mean MOA concentration was lowest in winter.



781 For the EYB region, northwesterly winds prevailed In DJF and SON and turned to northeasterly
782 winds over marginal seas of southeast China (Figure 9b and 9e), which transported MOA from the
783 major MPOA source region (EYB) to the northern part of the South China Sea (Figure 8b and 8e). As
784 wind speed over the EYB was low in MAM and JJA (Figure 9c and 9d, Table 9), MOA was mainly
785 restricted within this region (Figure 8c and 8d). In terms of seasonal average, MOA concentration
786 experienced its maximum in MAM, followed by those in DJF and SON, and the minimum in JJA
787 (Figure 8b~8e). The seasonal and regional mean MOA concentrations over the EYB were $0.62 \mu\text{g m}^{-3}$,
788 $0.54 \mu\text{g m}^{-3}$, $0.52 \mu\text{g m}^{-3}$, and $0.22 \mu\text{g m}^{-3}$ for MAM, DJF, SON, and JJA, respectively (Table 8). The
789 different seasonality between MOA concentration (Table 8) and MPOA emission (Table 7) in the EYB
790 region could also be mainly attributed to meteorological conditions. The MPOA emission was
791 relatively low in MAM (Table 7), but the second lowest wind speed and less precipitation (Table 9)
792 favored aerosol accumulation, resulting in the highest MOA concentration in spring (Table 8). The
793 minimum MPOA emission and the maximum precipitation in JJA led to the minimum MOA
794 concentration in summer. Although MPOA emission was largest in SON and DJF (Table 7), the
795 maximum wind speeds (Table 9) led to stronger dry deposition of aerosols and thus a moderate MOA
796 concentration in the two seasons (Table 8).

797 MOA concentration over the NWP region exhibited apparent higher concentrations in MAM and
798 JJA than those in SON and DJF (Figure 8b~8e), with the regional and seasonal averages reaching 0.81
799 $\mu\text{g m}^{-3}$ in MAM, $0.80 \mu\text{g m}^{-3}$ in JJA, $0.52 \mu\text{g m}^{-3}$ in SON, and $0.23 \mu\text{g m}^{-3}$ in DJF, respectively (Table
800 8). Using GEOS-Chem with a different marine organic aerosol emission scheme, Spracklen et al.
801 (2008) also showed that in the North Atlantic along the similar latitude bands to the NWP ($\sim 35^{\circ}\text{N}$ to
802 $\sim 55^{\circ}\text{N}$), both observation and simulation exhibited higher OC concentrations in summer and spring
803 than in the other seasons at the Azores Island and Mace Head Island. The strong seasonality of MOA
804 over the NWP was also attributed to the combined effects of MPOA emission, wind speed, and
805 precipitation. In MAM, the high MOA concentration over the NWP was mainly due to the large
806 MPOA emission (Figure 7c and Table 7), which was just smaller than that in SON, and partly due to
807 the relatively weak dry deposition and wet scavenging caused by moderate wind speed and
808 precipitation in this season (Table 9). In JJA, although the MPOA emission was small, the lowest wind
809 speed and precipitation in JJA over the NWP (2.5 m s^{-1} and $3.7 \text{ cm grid}^{-1} \text{ month}^{-1}$, Table 9) led to the
810 weakest dry deposition and wet scavenging of particles in summer, resulting in a long residence time



811 of MOA and consequently the high MOA concentration in summer over the NWP. In SON, although
812 the MPOA emission was largest over the NWP (Table 7), the mean wind speed was high over the
813 northern part of the NWP (Figure 9e) where MPOA emission mainly occurred (Figure 7e), leading to
814 strong dilution of MOA particles in autumn. Furthermore, the secondly largest precipitation over the
815 NWP in SON (Table 9) caused strong wet scavenging of particles, also contributed to the relatively
816 low MOA level. In DJF, the wind speed was largest, about 2 times those in the other seasons, and the
817 precipitation was also the maximum (Table 9, Figure 9b and 9g), leading to the lowest MOA
818 concentration in winter over the NWP (Figure 8b and Table 8).

819 As shown in Figures 8k~8o, MOA generally accounted for approximately 30% to over 60% of
820 total OA concentration over the remote oceans of high ($>35^{\circ}\text{N}$) and low ($<25^{\circ}\text{N}$) latitudes. The large
821 MOA/OA ratios over the remote oceans of high latitude (including NWP) could be attributed to the
822 high MOA concentration due to large marine emissions there; whereas, the large MOA/OA ratios over
823 the subtropical oceans of low latitude were mainly due to the low total OA level (small denominator).
824 Averaged over the NWP region, the annual mean MOA/OA ratio was 42%, with higher contributions
825 in MAM (52%) and SON (48%) and lower ones in DJF (36%) and JJA (32%) (Table 8). Although
826 MOA concentration over the NWP was secondly highest in JJA, its contribution was small because
827 OA transported from land sources also subject to weak dry deposition and wet scavenging, which led
828 to higher OA level and lower MOA/OA ratio. Over the EYB region, MOA accounted for
829 approximately 6% to 30% of the total OA in terms of annual mean (Figures 8k). In terms of annual
830 and regional average, the MOA/OA ratio was 13%, with higher ratios in SON (18%) and MAM (15%),
831 a moderate one in DJF (11%), and the lowest one in JJA (6%) (Table 8), similar to the seasonality over
832 the NWP. For the oceanic areas, the domain and annual mean MOA/OA ratio was 26%, indicating an
833 important contribution of MOA to airborne OA over the western Pacific. It was found that the
834 importance of MOA in total OA increased as the distance to the East Asian continent increased over
835 the western Pacific. It is also interesting to note that MOA even accounted for approximately 2~6% of
836 the annual mean OA mass over portions of southeast China (Figures 8k), and such contribution could
837 be as high as 8~10% in the coastal areas in SON (Figures 8o) and MAM (Figures 8m).

838 In all, both the MOA concentration and the MOA contribution to total OA were lowest in summer
839 (JJA) in the EYB region, which was mainly due to the much smaller MPOA emission in this season.
840 However, in the NWP region, although the MPOA emission was also lowest in summer, MOA



841 concentration in summer was in a same level as that in spring, and larger than those in the other
842 seasons, because dry deposition velocity and precipitation were lowest in summer, which favored
843 aerosol accumulation and a high level of MOA.

844 SOA produced by marine biogenic VOCs (isoprene and terpene) was on the order of 10^{-2} ~ 10^{-3} μg
845 m^{-3} (Figure 8f~8j), which was much lower than the MPOA concentration. The spatial distribution of
846 MSOA exhibited high concentrations over the EYB and NWP regions in terms of annual mean, with
847 values up to 6 ng m^{-3} (approximately 0.5% of MOA concentration) over these two regions (Figure 8f).
848 MSOA concentration exhibited the maximum in JJA, with seasonal mean values of $\sim 7 \text{ ng m}^{-3}$ to ~ 11
849 ng m^{-3} extending from the marginal seas of China (EYB) to remote western North Pacific (NWP)
850 (Figure 8i). MSOA distribution in MAM was similar to that in JJA but with lower mean
851 concentrations ($4\sim 7 \text{ ng m}^{-3}$) over the EYB and NWP regions (Figure 8h). In SON (Figure 8j), MSOA
852 concentrations were $2\sim 4 \text{ ng m}^{-3}$ in the above two regions. In DJF (Figure 8g), MSOA concentration
853 was lowest, with values of $0.4\sim 2 \text{ ng m}^{-3}$ over the marginal seas of China and the southern parts of the
854 western Pacific. The maximum seasonal mean MSOA concentration was up to 14 ng m^{-3} over oceanic
855 areas of the EYB to NWP regions in JJA, and the maximum daily mean MSOA value exceeded 28 ng
856 m^{-3} on some days, e.g. June 6~7 (figure not shown). Table 8 shows the domain and seasonal/annual
857 averages of MSOA over the oceanic regions of concern. The annual mean MSOA concentrations were
858 2.2 ng m^{-3} , 4.1 ng m^{-3} and 3.8 ng m^{-3} averaged over the western Pacific, the EYB and NWP regions. It
859 is striking that the domain average MSOA concentration consistently exhibited a distinct seasonality,
860 with the maximum in summer and the minimum in winter throughout all the oceanic regions of the
861 western Pacific, which was resulted from the combined effects of isoprene emission flux and
862 meteorological conditions. The domain average MSOA concentrations reached the maximums of 3.9
863 ng m^{-3} , 7.5 ng m^{-3} , and 8.3 ng m^{-3} , respectively, over the western Pacific, the EYB and NWP regions
864 in JJA. The seasonality of MSOA concentration over the western Pacific is similar to the simulation
865 result from Myriokefalitakis et al. (2010). According to Table 8, the annual mean fraction of MSOA
866 in MOA was estimated to be 0.8%, 0.9% and 0.6%, over the western Pacific, the EYB and NWP
867 regions, respectively. The maximum and minimum fractions of MSOA in MOA averaged over the
868 western Pacific occurred in JJA (1.7%) and DJF (0.3%), respectively, with the maximum regional and
869 seasonal average MSOA fraction up to 3.4% in summer over the EYB region. Based on the
870 GEOS-Chem model simulation, Arnold et al. (2009) indicated that SOA produced by marine isoprene



871 contributed only a very small fraction (0.01~1.4%) of the observed organic aerosol mass at remote
872 marine sites (Amsterdam Island in southern Indian Ocean, Azores and Mace Head islands in northern
873 Atlantic Ocean). In a global model simulation from Myriokefalitakis et al. (2010), the annual mean
874 marine isoprene and monoterpene derived SOA concentrations were approximately $0.4\sim 1\text{ ng m}^{-3}$
875 (accounting for ~0.4% of marine OA) over the western Pacific. Meskhidze et al. (2011) illustrated the
876 marine SOA from phytoplankton-derived isoprene and monoterpenes contributed <10% of surface
877 OM concentration of marine source in most areas of the western Pacific.

878

879 4.3 Direct radiative effect due to MOA

880 In this section, the direct radiative effect (DRE) due to MOA (DRE_{MOA}) over the western Pacific
881 of East Asia was estimated and analyzed. DRE is defined as the difference in net shortwave radiation
882 flux at TOA (or at the surface) induced by aerosols. The DRE of MOA is derived by the difference
883 between two radiation calls with all aerosols and with all aerosols but MOA (i.e., call two times in the
884 radiation module in the same simulation), reflecting an instantaneous change in shortwave radiation
885 fluxes induced by MOA. DRE of other aerosol components is estimated by using the same method.

886 Figures 10a to 10e show the annual and seasonal mean DRE_{MOA} at TOA under all-sky condition.
887 MOA induced negative DRE over the entire western Pacific. Consistent with the spatial distribution of
888 MOA concentration, the maximum DRE_{MOA} up to -0.9 W m^{-2} occurred over the NWP region (Figure
889 10a). Over the EYB region, the other hotspot of MOA mass concentration, the DRE_{MOA} was weaker,
890 with an annual mean DRE_{MOA} of $\sim -0.4\text{ W m}^{-2}$ (Figure 10a). In terms of domain average, the annual
891 mean DRE_{MOA} was estimated to be -0.27 W m^{-2} over the western Pacific, smaller than that over the
892 NWP (-0.50 W m^{-2}) but similar to that over the EYB (-0.33 W m^{-2}) (Table 10). The weaker DRE_{MOA}
893 over the EYB than that over the NWP could be attributed to both the lower MOA concentration (Table
894 8) and lower relative humidity (73% vs 83%, Table 9). The mean DRE_{MOA} over the western Pacific
895 was largest in spring (-0.38 W m^{-2}) and lowest in winter (-0.18 W m^{-2}) (Table 10), consistent with the
896 seasonality of MOA concentration.

897 In the NWP region, MOA induced the largest DRE up to -2.0 W m^{-2} to the northeast of Japan in
898 MAM (Figure 10c) and followed by that in JJA (up to -1.5 W m^{-2}) (Figure 10d) mainly due to higher
899 MOA concentrations in the two seasons. The DRE_{MOA} value was relatively low in SON ($\sim -0.7\text{ W m}^{-2}$)
900 (Figure 10e), and it was lowest in DJF, with the maximum of just -0.4 W m^{-2} (Figure 10b) due to the



901 lowest MOA concentration in winter (Table 8). The regional and seasonal means of DRE_{MOA} over the
902 NWP were estimated to be -0.76 W m^{-2} , -0.72 W m^{-2} , -0.32 W m^{-2} , and -0.21 W m^{-2} in MAM, JJA,
903 SON, and DJF, respectively (Table 10). On the contrary, in the EYB region, DRE_{MOA} exhibited a
904 different seasonal trend from that over the NWP, exhibiting the largest DRE in SON (Figure 10e),
905 moderate DREs in MAM (Figure 10c) and DJF (Figure 10b), and the lowest one in JJA (Figure 10d),
906 with corresponding mean values of -0.38 W m^{-2} , -0.34 W m^{-2} , -0.32 W m^{-2} , and -0.26 W m^{-2} ,
907 respectively, for the four seasons (Table 10).

908 It is of interest to estimate the relative importance of MOA in directly perturbing solar radiation
909 compared with other types of aerosols over the western Pacific. Table 10 lists the simulated annual
910 and seasonal mean DREs due to sea salt and anthropogenic aerosols over the western Pacific and the
911 regions of NWP and EYB, respectively. It is noted that the annual mean DRE_{MOA} was approximately
912 one third of that due to sea salt and one order of magnitude lower than that due to anthropogenic
913 aerosols on average over the western Pacific. Over the EYB region, DRE_{MOA} was almost negligible
914 compared with that by anthropogenic aerosols due to the predominance of anthropogenic emissions
915 near the continent, however, it is noteworthy that DRE_{MOA} was comparable in magnitude to the DRE
916 by sea salt, especially in springtime (-0.34 vs -0.36 W m^{-2} in MAM) when MOA concentration
917 reached its maximum (Table 8). Over the remote oceans (NWP), DRE_{MOA} was approximately 19% of
918 the DRE by anthropogenic aerosols due to weakened influence of continental anthropogenic emissions
919 over open oceans, and it was comparable in magnitude to the DRE by sea salt, especially in
920 summertime (0.72 vs 0.79 W m^{-2}) when sea salt emission flux was lowest (Table 7). The annual and
921 regional mean all-sky DRE_{MOA} were approximately 10%, 5%, and 19% of the DREs due to
922 anthropogenic aerosols over the western Pacific, the EYB, and NWP, respectively, and it was
923 comparable in magnitude to the DREs by sea salt in the EYB and NWP regions.

924 It should be mentioned that due to the much smaller MSOA concentration than MPOA
925 concentration, the above DRE_{MOA} was dominantly contributed by MPOA, similar to the findings from
926 previous studies (Arnold et al., 2009; Booge et al., 2016; Li et al., 2019). MPOA also dominated over
927 MSOA in the following IRE estimation.

928

929 4.4 Indirect radiative effect due to MOA

930 The first indirect effect refers to that aerosol particles tend to increase cloud droplet number



931 concentration, decrease cloud effective radius under stable cloud liquid water content, and thus
932 modify cloud optical properties and radiation, which is also denoted as the indirect radiative effect
933 (IRE) in this study. IRE due to marine organic aerosols (IRE_{MOA}) over the western Pacific of East Asia
934 was explored in this section. The first indirect radiative effect or IRE of MOA is estimated by the
935 instantaneous difference in net shortwave radiation flux at TOA (or at the surface) between two
936 radiation calls with all aerosols and with all aerosols but MOA in one simulation. The lower bound of
937 cloud droplet number concentration (N_c) is set to $10/cm^3$, which roughly represents N_c in liquid clouds
938 in clean ocean conditions, according to satellite observations and global simulations. Hoose et al.
939 (2009) pointed out that the choice of low bound of N_c may lead to uncertainties in IRE estimation. The
940 IRE calculation in this study can be written as follows:

$$941 \quad IRE_{ai} = (F_{\downarrow} - F_{\uparrow})_{all\ aerosols} - (F_{\downarrow} - F_{\uparrow})_{all\ aerosols\ but\ at}$$

942 Here F_{\downarrow} and F_{\uparrow} represents incoming and outgoing shortwave radiation fluxes, respectively, a_i denotes
943 a specific aerosol component, e.g., MOA. Here, the calculation of IRE due to MOA (the sum of
944 MPOA and MSOA) is called the base case (BASE), from which a series of sensitivity simulations are
945 carried out below.

946 N_c due to aerosol activation is diagnosed by the A-G scheme, then the cloud effective radius r_c is
947 calculated as a function of N_c and cloud liquid water content following the approach of Martin et al.
948 (1994), and the cloud optical parameters (liquid cloud extinction optical depth, single scatter albedo,
949 asymmetry factor etc.) are calculated by the scheme of Slingo et al. (1989), finally, shortwave
950 radiation fluxes are calculated by the CCM3 radiation scheme (Kiehl et al., 1996).

951 The annual and seasonal mean IRE_{MOA} at TOA are shown in Figure 10f to 10j. IRE_{MOA} was
952 negative in the entire domain, resulting from a series of changes in cloud properties induced by MOA,
953 i.e., an increase in cloud droplet number concentration, a decrease in cloud droplet effective radius, an
954 increase in cloud optical depth and cloud water path, and consequently more reflection of solar
955 radiation at TOA. The model simulated cloud properties have been compared against satellite
956 retrievals in spring 2014 in our previous study (Han et al., 2019), which indicated the model was able
957 to reasonably reproduce the major features of cloud distribution. It is remarkable that IRE_{MOA} was
958 stronger than DRE_{MOA} over the western Pacific, with the maximum annual mean of IRE_{MOA} being
959 approximately three times the maximum of DRE_{MOA} , and the positions of their maximum values were
960 different. The annual mean IRE_{MOA} of $-0.9 \sim -2.5 \text{ W m}^{-2}$ distributed from southwest to northeast over



961 wide areas of the western Pacific (Figure 10f). It was evident that the strongest IRE_{MOA} occurred in
962 spring (MAM), with the seasonal mean values of $-1.2 \sim -3.0 \text{ W m}^{-2}$ over vast areas from the East
963 China Sea to the oceans east of Japan (Figure 10h). IRE_{MOA} in SON was similar in distribution pattern
964 to that in MAM, with lower values in these regions (Figure 10j). The IRE_{MOA} was weakest in JJA,
965 with the maximum up to -1.5 W m^{-2} over a portion of the western Pacific east of Japan (Figure 10i),
966 whereas the IRE_{MOA} value in DJF was between those in MAM and JJA with a similar distribution
967 pattern. The seasonal variation of IRE_{MOA} was likely influenced by both the seasonal changes in cloud
968 amount and MOA concentration. In terms of domain average, the seasonal mean IRE_{MOA} was
969 strongest (-0.94 W m^{-2}) in MAM over the western Pacific (Table 10), which was mainly attributed to
970 the maximum MOA concentration in spring (Table 8). IRE_{MOA} was secondly strongest in SON (-0.7
971 W m^{-2}) because MOA concentration and cloud fraction (Figure S3j) were both high in autumn. The
972 weakest IRE_{MOA} occurred in JJA, which was mainly attributed to both the lower MOA concentration
973 and cloud fraction in summer (Table 8, Figure S3i). Figure S4 further presents the monthly mean
974 distributions of Chl-a concentration, MPOA emission, MOA concentration, and IRE_{MOA} in April,
975 when Chl-a concentration and MPOA emission resulting from phytoplankton were distinctly high in
976 the EYB and NWP regions (Figure S4a and S4b). It can be found that MOA was transported from the
977 high Chl-a regions to the southeast under northwesterly winds over the oceans (Figure S4c), resulting
978 in an elevated IRE_{MOA} up to -5 W m^{-2} over the western Pacific east of Japan (Figure S4d). Previous
979 studies were very limited to compare with. Meskhidze and Nenes (2006) estimated based on satellite
980 retrievals a reduction of 15 W m^{-2} in shortwave radiation at TOA due to changes in cloud properties
981 during a strong phytoplankton bloom event near South Georgia Island in the Southern Ocean in
982 summertime.

983 In terms of annual and regional mean, IRE_{MOA} was estimated to be -0.66 W m^{-2} for the western
984 Pacific, -0.23 W m^{-2} over the EYB region, and -1.04 W m^{-2} over the NWP region, respectively (Table
985 10). There was an apparent seasonality in the IRE_{MOA} , with the maximum of -0.94 W m^{-2} in MAM and
986 the minimum of -0.36 W m^{-2} in JJA over the western Pacific (Table 10). However, the seasonality of
987 IRE_{MOA} in the EYB and NWP regions are different from that over the western Pacific. Over the EYB,
988 the estimated IRE_{MOA} reached its maximum (-0.38 W m^{-2}) in SON, which was due to the combined
989 effect of a moderately high MOA concentration (Table 8) and the maximum cloud fraction (Figure S3j)
990 in this region. Although MOA concentration reached the maximum in MAM, there was a minimum



991 total cloud fraction in spring among seasons (Figure S3h), leading to a moderate IRE_{MOA} . Over the
992 NWP region, IRE_{MOA} in DJF (-0.57 W m^{-2}) was smaller than those in other seasons ($-0.78 \sim -1.4 \text{ W}$
993 m^{-2}), which was mainly attributed to the lowest MOA concentration in winter (Table 8), although
994 cloud fraction was highest among seasons in this region (Figure S3g).

995 The relative importance of MOA in the aerosol indirect radiative effect over the western Pacific
996 was investigated by comparing the IRE_{MOA} with the IREs induced by sea salt and anthropogenic
997 aerosols. In terms of annual and oceanic average, the IREs by sea salt and anthropogenic aerosols
998 were estimated to be -0.41 W m^{-2} and -7.7 W m^{-2} (Table 10), respectively, indicating IRE_{MOA} (-0.66 W
999 m^{-2}) was larger than the IRE by sea salt and was approximately 9% of that by anthropogenic aerosols.
1000 It is noted that the relative magnitude of IRE_{MOA} compared with the IRE by anthropogenic aerosols
1001 was reduced (5%) in the EYB and enhanced over the NWP (12%), because anthropogenic aerosols
1002 from the East Asian continent dominated aerosol magnitude in the marginal seas of China. In terms of
1003 seasonal and domain average over the western Pacific, IRE_{MOA} was approximately 1.6 times the IRE
1004 by sea salt, and approximately 10% of the IRE by anthropogenic aerosols in MAM. In summer (JJA)
1005 when both sea salt and anthropogenic aerosol concentrations were lowest, IRE_{MOA} was similar in
1006 magnitude to the IRE by sea salt, and about 8% of the IRE by anthropogenic aerosols. In the EYB
1007 region, IRE_{MOA} was just about 5% of the IRE by anthropogenic aerosols, but approximately three
1008 times the IRE by sea salt. In the NWP, IRE_{MOA} was about 12% of the IRE by anthropogenic aerosols
1009 in terms of annual mean, whereas in autumn when anthropogenic aerosol level was relatively low,
1010 IRE_{MOA} was as high as the maximum in MAM and approximately 18% of the IRE by anthropogenic
1011 aerosols. The above model estimation demonstrates that IRE_{MOA} was generally stronger than the IRE
1012 due to sea salt over the western Pacific, and approximately 6~18% of the IRE due to anthropogenic
1013 aerosols in the four seasons over the NWP, suggesting an important role of MOA in perturbing
1014 radiation transfer through modifying cloud properties over the western Pacific Ocean of East Asia.
1015 The estimated IRE due to MSOA accounted for approximately 1% of the annual mean IRE_{MOA}
1016 averaged over the western Pacific, consistent with the very low proportion of MSOA in the MOA
1017 mass concentration (Table 8). Overall, MSOA plays a minor role in perturbing cloud properties and
1018 shortwave radiation compared with MPOA.

1019 To address potential uncertainty in the estimated IRE_{MOA} due to limited knowledge on MOA
1020 properties, three additional sensitivity simulations from the base case (results shown in Figure S5 and



1021 Table S4) were carried out regarding particle size, solubility, and molecule weight, which are crucial
1022 to aerosol activation (note we focus on MPOA due to its dominant fraction in MOA as shown above).
1023 The first sensitivity simulation (SENS1) assumes a smaller geometric mean radius ($0.02\mu\text{m}$ instead of
1024 $0.05\mu\text{m}$ in the base case) for MPOA, resulting in a weaker domain-annual mean IRE_{MOA} (-0.53 W m^{-2})
1025 than that in the base case (-0.66 W m^{-2}) over the oceanic region (Figure S5b, Table S4). The second
1026 sensitivity simulation (SENS2) assigns a lower solubility (0.05) with relatively large molecule weight
1027 (146 g mol^{-1}) for MPOA (which is similar to the properties of adipic acid, Huff Hartz et al., 2006;
1028 Miyazaki et al., 2010) instead of the slight solubility (0.1) with a smaller molecule weight (90 g mol^{-1})
1029 (which is similar to the properties of oxalic acid, Roelofs, 2008; Miyazaki et al., 2010) in the base case,
1030 in this case, the IRE_{MOA} reduces to -0.2 W m^{-2} (Figure S5c, Table S4). The third simulation (SENS3)
1031 combines the above two cases, assuming a smaller geometric mean radius as in SENS1 together with
1032 the lower solubility and larger molecule weight as in SENS2, it produces a further reduced IRE_{MOA} of
1033 0.14 W m^{-2} (Figure S5d, Table S4). The above sensitivity simulations exhibit a high sensitivity of
1034 IRE_{MOA} to the MPOA properties.

1035 It is interesting to note that Quinn et al. (2017) indicated that sea spray aerosol generally makes a
1036 contribution of less than 30% to CCN population at supersaturation of 0.1 to 1.0% on a global basis
1037 based on measurements onboard seven research cruises over the Pacific, Southern, Arctic and Atlantic
1038 oceans. However, their cruise tracks did not cover the western Pacific Ocean. The results from this
1039 study exhibits the annual and oceanic mean contribution of sea spray aerosol (the sum of MOA and
1040 sea salt) to the IRE by all aerosols (the sum of MOA, sea salt and anthropogenic aerosols) was
1041 approximately 12% in the base case over the western Pacific region (Table 10). This percentage
1042 contribution increases to 19% in the NWP in autumn due to the highest IRE_{MOA} and lower IRE by
1043 anthropogenic aerosols in autumn (Table 10).

1044 The western Pacific Ocean is just downwind of the East Asian continent, which have large
1045 amounts of anthropogenic aerosols, mineral dust, and nutrients inputs to the marginal seas of China
1046 from the Yangtze and Yellow Rivers, could be very different from remote clean oceans in the world.
1047 Although some cruise measurements have been carried out and a few knowledges on MOA properties
1048 (e.g., size distribution) was gained, the cruise measurement and observational analysis for MOA
1049 chemical properties are so far almost absent in the western Pacific of East Asia. Therefore, marine
1050 biogeochemistry, marine aerosol sources and properties, as well as their potentials to be CCN and



1051 impacts on radiation, cloud, and precipitation deserve further investigation in the future.

1052

1053 4.5 Indirect radiative effect of MOA due to aerosol-radiation and aerosol-cloud interactions

1054 IPCC AR5 proposes the concept of effective radiative forcing (ERF), which is defined as the
1055 change in net radiative flux at TOA after rapid adjustment of the atmosphere (including atmospheric
1056 temperature, water vapor, cloud, circulation) to radiation perturbation with prescribed SST and sea ice,
1057 which can better represent climate response to perturbation of forcing factors (Boucher et al., 2013).

1058 Similarly, this study also estimates the direct radiative effect of MOA due to aerosol-radiation
1059 interaction (denoted as DRE_{ari} hereinafter) and the indirect radiative effect of MOA due to
1060 aerosol-cloud interaction (denoted as IRE_{aci} hereinafter), which consider the adjustment of
1061 atmospheric temperature, water vapor, and cloud (including cloud microphysical and lifetime change,
1062 i.e., the second indirect effect) to the MOA-induced radiation perturbation. DRE_{ari} is derived by the
1063 difference in shortwave radiation flux induced by MOA scattering at TOA between two simulations
1064 with all aerosols and with all aerosols but MOA, while the perturbation of MOA to cloud properties is
1065 turned off. IRE_{aci} is calculated by the difference in shortwave radiation flux resulting from changes in
1066 cloud albedo induced by MOA at TOA between the two simulations, while the perturbation of MOA
1067 to radiation is closed.

1068 Figure 11a shows the annual mean MOA DRE_{ari} in the study domain. It is noted that DRE_{ari} was
1069 not consistently negative in the domain, the effect of atmospheric adjustment on radiation can be seen
1070 in some locations over the Ocean and the continent, with a few positive values of $0.1\sim 0.3\text{ Wm}^{-2}$.

1071 Figure 11b shows the annual mean MOA IRE_{aci} in the study domain, which was similar in
1072 magnitude and distribution pattern to IRE_{MOA} (Figure 10f), but it distributed unevenly in the domain
1073 with some positive values exceeding 0.2 W m^{-3} over both the Western Pacific and the continent. The
1074 atmospheric response and adjustment induced by IRE_{MOA} could be somewhat stronger than that by
1075 DRE_{MOA} , given the positive values of IRE_{aci} up to 0.3 W m^{-3} over the continent. The small positive
1076 values could be associated with the radiative feedback and atmospheric and cloud adjustment.

1077 The annual and domain average of DRE_{ari} and IRE_{aci} over the western Pacific are estimated to be
1078 -0.25 Wm^{-2} and -0.61 W m^{-2} , respectively, both are somewhat weaker than the DRE_{MOA} (-0.27 Wm^{-2})
1079 and IRE_{MOA} (-0.66 Wm^{-2}), which could be due to the offset effect by the positive values.

1080



1081 5. Conclusions.

1082 The organic aerosols of marine origin over the western Pacific Ocean of East Asia was
1083 investigated by an online-coupled regional climate-chemistry model RIEMS-Chem for the year 2014.
1084 Emissions and relevant processes of marine MPOA, isoprene and monoterpene were incorporated into
1085 RIEMS-Chem. A wide variety of observational datasets from EANET, CNEMC and AERONET
1086 networks, cruise measurements and previous publications were collected for model validation. The
1087 modeled SOA from marine VOC sources was also compared with secondary organic tracers measured
1088 by research cruise. The model performed well for PM_{2.5} and PM₁₀ in marine environment, producing
1089 overall correlation coefficients and NMBs of 0.61/0.70 and 12%/-7% for PM_{2.5} concentration,
1090 0.65/0.65 and -5%/-1% for PM₁₀ concentration at the EANET/CNEMC sites, respectively. The model
1091 reasonably reproduced the spatial distribution and temporal variation of BC and OC concentrations
1092 along cruise tracks and at islands over the west Pacific, with the correlation coefficients and NMBs
1093 being 0.6~0.75 and -28%~3% for OC, respectively. The modeled OC concentration was apparently
1094 improved while taking into account marine organic aerosols. The model results clearly showed an
1095 increasing contribution of marine organic aerosols to total OC mass concentration from the marginal
1096 seas of China to remote oceans. Organic aerosol mass of marine origin was dominated by MPOA
1097 because MSOA produced by marine isoprene and monoterpene emissions was about 1~2 orders of
1098 magnitude lower than MPOA. The model simulates AOD reasonably well at the 7 coastal or island
1099 AERONET sites, with an overall correlation coefficient of 0.54 and an NMB of -6%.

1100 High MPOA emission mainly occurred over the marginal seas of China (EYB) and the northern
1101 parts of western Pacific northeast of Japan (NWP). For the western Pacific, MPOA emission reached
1102 the maximum in SON, followed by those in DJF and MAM, and the minimum in JJA, with an annual
1103 and domain average emission rate of $0.16 \times 10^{-2} \mu\text{g m}^{-2} \text{ s}^{-1}$. The combination of Chl-a concentration and
1104 sea salt emission flux determined the seasonality of MPOA emission. The annual MPOA emission for
1105 the year 2014 was estimated to be 0.78 Tg yr^{-1} over the western Pacific.

1106 Consistent with the distribution pattern MPOA emission, high MOA concentration mainly
1107 distributed over the EYB and NWP, with an annual and domain mean concentration of $0.27 \mu\text{g m}^{-3}$,
1108 $0.48 \mu\text{g m}^{-3}$ and $0.59 \mu\text{g m}^{-3}$, over the western Pacific, the EYB and NWP regions, respectively. MOA
1109 concentration was highest in MAM and lowest in DJF, with the seasonal and domain mean values of
1110 $0.37 \mu\text{g m}^{-3}$ and $0.21 \mu\text{g m}^{-3}$, respectively, over the western Pacific. The seasonality of MOA



1111 concentration was determined by the combined effect of MPOA emission, dry and wet depositions.

1112 On average, the annual mean percentage contribution of MOA to total OA mass was 26% over the
1113 western Pacific, with the largest seasonal mean contribution of 32% in SON and the lower ones in
1114 DJF (24%) and JJA (23%). Over the NWP, the domain average contribution of MOA to OA could be
1115 as high as 42% in terms of annual mean and approaching 52% in MAM; however, over the EYB, the
1116 annual mean contribution was just 13% and the percentage contribution was even reduced to 6% in
1117 JJA. This indicated that the relative importance of MOA in total OA concentration increased with the
1118 distance away from the East Asian continent. MSOA concentration was approximately 1~2 orders of
1119 magnitude lower than MPOA, with the simulated annual and regional mean MSOA being 2.2 ng m^{-3}
1120 and the maximum daily mean value up to 28 ng m^{-3} in summer over the western Pacific.

1121 An annual/oceanic mean all-sky DRE_{MOA} of -0.27 W m^{-2} at TOA was estimated over the western
1122 Pacific, which was about 40% of the IRE_{MOA} (-0.66 W m^{-2}). The domain mean IRE_{MOA} was strongest
1123 in spring (-0.94 W m^{-2}) and weakest in summer (-0.36 W m^{-2}) over the western Pacific, and the
1124 monthly mean IRE_{MOA} can reach -5 W m^{-2} in the NWP region east of Japan in April. The changes in
1125 MOA concentration and cloud amount both contributed to the seasonality of IRE_{MOA} . In terms of
1126 annual and oceanic mean over the western Pacific, MSOA just contributed approximately 1% of the
1127 IRE_{MOA} . IRE_{MOA} was generally larger than the IRE due to sea salt on average. The annual and oceanic
1128 mean IRE due to sea spray aerosols (MOA + sea salt) was approximately 12% of that due to all
1129 aerosols (anthropogenic + MOA + sea salt aerosols) over the western Pacific, but this ratio can
1130 increase up to 19% in autumn in the NWP region. The estimation of IRE_{MOA} was sensitive to MOA
1131 properties, which decreased apparently while a smaller geometric mean radius together with a lower
1132 solubility and a larger molecule weight were assigned for MOA. Overall, the indirect radiative effect
1133 of MOA was larger than the direct radiative effect, and had a nonnegligible impact on radiation budget
1134 and cloud over the western Pacific. The direct and indirect radiative effect considering atmospheric
1135 feedback and adjustment were estimated as well, which was similar in magnitude to the DRE_{MOA} and
1136 IRE_{MOA} , with a few positive changes in shortwave radiation fluxes in some locations.

1137 While this study presents new insights into the seasonal variation and annual means of emissions,
1138 concentrations, and radiative effects of MOA in the western Pacific, it is still subject to some
1139 uncertainties as follows: 1.) the properties of marine organic aerosols, including size distribution,
1140 molecular weight, solubility, surfactant amount etc. are still poorly characterized, which are crucial to



1141 aerosol activation, dry deposition, and wet scavenging; 2.) the sources and chemical formation
1142 processes of marine organic aerosols including secondary organics are highly complex, and poorly
1143 understood and represented in the model; 3.) the indirect effects of MOA in this study is for warm
1144 stratiform cloud. Further research on MOA sources, properties, chemical processes, and climatic
1145 impacts will be conducted together with the advances in both field experiments (integrated cruise,
1146 aircraft and satellite observations) and model development in the future.

1147

1148 **Author Contributions.**

1149 ZH designed the study, JL and ZH developed the model, processed and analyzed the model results, JL
1150 performed the model simulation, ZH and JL wrote the paper, PF and XY provided and analyzed the
1151 cruise measurement data.

1152

1153 **Data availability.**

1154 The observational data can be accessed through contacting the corresponding author.

1155

1156 **Competing interests.**

1157 The authors declare that they have no conflict of interests.

1158

1159 **Acknowledgement.**

1160 This study was supported by the National Key R&D Program of China (No. 2019YFA0606802),
1161 the National Natural Science Foundation of China (No. 42275118, No. 91644217), the Jiangsu
1162 Collaborative Innovation Center for Climate Change. The authors appreciate the science teams of
1163 EANET, CNEMC, AERONET, and VIIRS for their works in data maintenance.

1164

1165 **Reference**

- 1166 Abdul-Razzak, H., Ghan, S. J., and Rivera-Carpio, C.: A parameterization of aerosol activation: 1.
1167 Single aerosol type, *J. Geophys. Res.*, 103, 6123–6131, 1998.
- 1168 Abdul-Razzak, H. and Ghan, S. J.: Parameterization of the influence of organic surfactants on aerosol
1169 activation, *J. Geophys. Res.*, 109, D03205, doi:10.1029/2003JD004043, 2004.
- 1170 Arnold, S.R., Spracklen, D.V., Williams, J., Yassaa, N., Sciare, J., Bonsang, B., Gros, V., Peeken, I.,



- 1171 Lewis, A.C., Alvain, S., and Moulin, C.: Evaluation of the global oceanic isoprene source and its
1172 impacts on marine organic carbon aerosol, *Atmos. Chem. Phys.*, 9, 1253–1262.
1173 <https://doi.org/10.5194/acp-9-1253-2009>, 2009.
- 1174 Bates, T. S., Quinn, P. K., Coffman, D. J., Johnson, J. E., Upchurch, L., Saliba, G., Lewis, S., Graff, J.,
1175 Russell, L. M., and Behrenfeld, M. J.: Variability in Marine Plankton Ecosystems Are Not
1176 Observed in Freshly Emitted Sea Spray Aerosol Over the North Atlantic Ocean, *Geophys. Res.
1177 Lett.*, 47, e2019GL085938. <https://doi.org/10.1029/2019GL085938>, 2020.
- 1178 Beheng, K.D.: A parameterization of warm cloud microphysical conversion processes. *Atmos. Res.*,
1179 33, 193–206. [https://doi.org/10.1016/0169-8095\(94\)90020-5](https://doi.org/10.1016/0169-8095(94)90020-5), 1994.
- 1180 Bertram, T. H., Cochran, R. E., Grassian, V. H., and Stone, E. A.: Sea spray aerosol chemical
1181 composition: elemental and molecular mimics for laboratory studies of heterogeneous and
1182 multiphase reactions, *Chem. Soc. Rev.*, 47(7), 2374–2400, DOI: 10.1039/c7cs00008a, 2018.
- 1183 Bennartz, R.: Global assessment of marine boundary layer cloud droplet number concentration from
1184 satellite, *J. Geophys. Res.*, 112, D02201, doi:10.1029/2006jd007547, 2007.
- 1185 Bikkina, S., Kawamura, K., Miyazaki, Y., and Fu, P.: High abundances of oxalic, azelaic and glyoxylic
1186 acids and methylglyoxal in the open ocean with high biological activity: Implication for
1187 secondary OA formation from isoprene, *Geophys. Res. Lett.*, 41, 3649–3657, 2014.
- 1188 Booge, D., Marandino, C.A., Schlundt, C., Palmer, P.I., Schlundt, M., Atlas, E.L., Bracher, A.,
1189 Saltzman, E.S., and Wallace, D.W.R.: Can simple models predict large-scale surface ocean
1190 isoprene concentrations? *Atmos. Chem. Phys.*, 16, 11807–11821,
1191 <https://doi.org/10.5194/acp-16-11807-2016>, 2016.
- 1192 Boreddy, S.K.R., Haque, M.M., and Kawamura, K.: Long-term (2001–2012) trends of carbonaceous
1193 aerosols from a remote island in the western North Pacific: an outflow region of Asian pollutants,
1194 *Atmos. Chem. Phys.*, 18, 1291–1306, <https://doi.org/10.5194/acp-18-1291-2018>, 2018.
- 1195 Boucher, O., Randall, D., Artaxo, P., Bretherton, C., Feingold, G., Forster, P., et al.: Clouds and
1196 aerosols. In T. F. Stocker, et al. (Eds.), *Climate change 2013: The physical science basis.*
1197 *Contribution of working group I to the fifth assessment report of the Intergovernmental Panel on*
1198 *Climate Change* (pp. 616–632). Cambridge: Cambridge University Press, 2013.
- 1199 Brüggemann, M., Hayeck, N. and George, C.: Interfacial photochemistry at the ocean surface is a
1200 global source of organic vapors and aerosols, *Nat. Commun.*, 9, 2101.



- 1201 <https://doi.org/10.1038/s41467-018-04528-7>, 2018.
- 1202 Burrows, S. M., Ogunro, O., Frossard, A. A., Russell, L. M., Rasch, P. J., and Elliott, S. M.: A
1203 physically based framework for modeling the organic fractionation of sea spray aerosol from
1204 bubble film Langmuir equilibria, *Atmos. Chem. Phys.*, 14, 13601–13629,
1205 <https://doi.org/10.5194/acp-14-13601-2014>, 2014.
- 1206 Burrows, S. M., Easter, R. C., Liu, X., Ma, P.-L., Wang, H., Elliott, S. M., Singh, B., Zhang, K., and
1207 Rasch, P. J.: OCEANFILMS (Organic Compounds from Ecosystems to Aerosols: Natural Films
1208 and Interfaces via Langmuir Molecular Surfactants) sea spray organic aerosol emissions –
1209 implementation in a global climate model and impacts on clouds, *Atmos. Chem. Phys.*, 22, 5223–
1210 5251, <https://doi.org/10.5194/acp-22-5223-2022>, 2022.
- 1211 Calil, P.H.R., Doney, S.C., Yumimoto, K., Eguchi, K., Takemura, T.: Episodic upwelling and dust
1212 deposition as bloom triggers in low-nutrient, low-chlorophyll regions, *J. Geophys. Res.: Oceans*,
1213 116, C06030. <http://dx.doi.org/10.1029/2010JC006704>, 2011.
- 1214 Chang, J.S., Brost, R.A., Isaksen, I.S.A., Madronich, S., Middleton, P., Stockwell, W.R., Walcek, C.J.:
1215 A three-dimensional Eulerian acid deposition model: physical concepts and formulation, *J.*
1216 *Geophys. Res.*, 92(D12), 14681-14700, doi:10.1029/JD092iD12p14681, 1987.
- 1217 Conte, L., Szopa, S., Aumont, O., Gros, V., and Bopp, L.: Sources and sinks of isoprene in the global
1218 open ocean: Simulated patterns and emissions to the atmosphere, *J. Geophys. Res: Oceans*, 125,
1219 e2019JC015946. <https://doi.org/10.1029/2019JC015946>, 2020.
- 1220 Curci, G., Hogrefe, C., Bianconi, R., Im, U., Balzarini, A., Baró, R., Brunner, D., Forkel, R., Giordano,
1221 L., Hirtl, M., Honzak, L., Jiménez-Guerrero, P., Knote, C., Langer, M., Makar, P. A., Pirovano, G.,
1222 Pérez, J. L., San José, R., Syrakov, D., Tuccella, P., Werhahn, J., Wolke, R., Žabkar, R., Zhang, J.,
1223 and Galmarini, S.: Uncertainties of simulated aerosol optical properties induced by assumptions
1224 on aerosol physical and chemical properties: An AQMEII-2 perspective, *Atmos. Environ.*, 115,
1225 541–552, 2015.
- 1226 Dickinson, R.E., Henderson-Sellers, A., Kennedy, P.J.: Biosphere-Atmosphere Transfer Scheme
1227 (BATS) Version 1e as coupled to NCAR Community Climate Model, NCAR Technical Note,
1228 NCAR/TN-387+STR, p. 72, 1993.
- 1229 Emmons, L.K., Walters, S., Hess, P.G., Lamarque, J.-F., Pfister, G.G., Fillmore, D., Granier, C.,
1230 Guenther, A., Kinnison, D., Laepple, T., Orlando, J., Tie, X., Tyndall, G., Wiedinmyer, C.,



- 1231 Baughcum, S.L., and Kloster, S.: Description and evaluation of the Model for Ozone and Related
1232 chemical Tracers, version 4 (MOZART-4), *Geosci. Model Dev.*, 3, 43-67,
1233 doi:10.5194/gmd-3-43-2010, 2010.
- 1234 Facchini, M.C., Rinaldi, M., Decesari, S., Carbone, C., Finessi, E., Mircea, M., Fuzzi, S., Ceburnis, D.,
1235 Flanagan, R., Nilsson, E.D., de Leeuw, G., Martino, M., Woeltjen, J., and O'Dowd, C.D.:
1236 Primary submicron marine aerosol dominated by insoluble organic colloids and aggregates,
1237 *Geophys. Res. Lett.*, 35, L17814, doi:10.1029/2008GL034210, 2008.
- 1238 Feng, L.M., Shen, H.Q., Zhu, Y.J., Gao, H.W., and Yao, X.H.: Insight into Generation and Evolution
1239 of Sea-Salt Aerosols from Field Measurements in Diversified Marine and Coastal Atmospheres,
1240 *Sci. Rep.*, 7, 41260; doi: 10.1038/srep41260, 2017.
- 1241 Fountoukis, C. and Nenes, A.: ISORROPIA II: a computationally efficient thermodynamic
1242 equilibrium model for K^+ - Ca^{2+} - Mg^{2+} - NH_4^+ - Na^+ - SO_4^{2-} - NO_3^- - Cl^- - H_2O aerosols, *Atmos. Chem.*
1243 *Phys.*, 7, 4639-4659, 2007.
- 1244 Fröhlich-Nowoisky Janine, Christopher J. Kampf, Bettina Weber, J. Alex Huffman, Christopher
1245 Pöhlker, Meinrat O. Andreae, Naama Lang-Yona, Susannah M. Burrows, Sachin S. Gunthe,
1246 Wolfgang Elbert, Hang Su, Peter Hoor, Eckhard Thines, Thorsten Hoffmann, Viviane R. Després,
1247 Ulrich Pöschl: Bioaerosols in the Earth system: Climate, health, and ecosystem interactions.
1248 *Atmospheric Research*, 182, 346-376, 2016.
- 1249 Fu, C. B., Wang, S.Y., Xiong, Z., Gutowski, W. J., Lee, D., McGregor, J. L., Sato, Y., Kato, H., Kim, J.,
1250 Suh, M.: Regional climate model intercomparison project for Asia, *Bull. Amer. Meteor. Soc.*, 86,
1251 257-266, 2005.
- 1252 Fu, P., Kawamura, K., and Miura, K.: Molecular characterization of marine organic aerosols collected
1253 during a round - the - world cruise, *J. Geophys. Res.*, 116, D13302, doi:10.1029/2011JD015604,
1254 2011.
- 1255 Gantt, B., Meskhidze, N., and Kamykowski, D.: A new physically-based quantification of marine
1256 isoprene and primary organic aerosol emissions, *Atmos. Chem. Phys.*, 9, 4915-4927,
1257 <https://doi.org/10.5194/acp-9-4915-2009>, 2009.
- 1258 Gantt, B., Meskhidze, N., Facchini, M.C., Rinaldi, M., Ceburnis, D., and O'Dowd, C.D.: Wind speed
1259 dependent size-resolved parameterization for the organic mass fraction of sea spray aerosol,
1260 *Atmos. Chem. Phys.*, 11, 8777-8790, <https://doi.org/10.5194/acp-11-8777-2011>, 2011.



- 1261 Gantt, B., Johnson, M. S., Meskhidze, N., Sciare, J., Ovadnevaite, J., Ceburnis, D., and O'Dowd, C. D.:
1262 Model evaluation of marine primary organic aerosol emission schemes, *Atmos. Chem. Phys.*, 12,
1263 8553-8566, <https://doi.org/10.5194/acp-12-8553-2012>, 2012a.
- 1264 Gantt, B., Xu, J., Meskhidze, N., Zhang, Y., Nenes, A., Ghan, S. J., Liu, X., Easter, R., and Zaveri, R.:
1265 Global distribution and climate forcing of marine organic aerosol – Part 2: Effects on cloud
1266 properties and radiative forcing, *Atmos. Chem. Phys.*, 12, 6555-6563,
1267 <https://doi.org/10.5194/acp-12-6555-2012>, 2012b.
- 1268 Gantt, B. and Meskhidze, N.: The physical and chemical characteristics of marine primary organic
1269 aerosol: a review, *Atmos. Chem. Phys.*, 13, 3979–3996, 2013.
- 1270 Gao, M., Han, Z., Liu, Z., Li, M., Xin, J., Tao, Z., Li, J., Kang, J.-E., Huang, K., Dong, X., Zhuang, B.,
1271 Li, S., Ge, B., Wu, Q., Cheng, Y., Wang, Y., Lee, H.-J., Kim, C.-H., Fu, J. S., Wang, T., Chin, M.,
1272 Woo, J.-H., Zhang, Q., Wang, Z., and Carmichael, G. R.: Air quality and climate change, Topic 3
1273 of the Model Inter-Comparison Study for Asia Phase III (MICS-Asia III) – Part 1: Overview and
1274 model evaluation, *Atmos. Chem. Phys.*, 18, 4859-4884, 2018.
- 1275 Gery, M. W., Whitten, G. Z., Killus, J. P., Dodge, M. C.. A photochemical kinetics mechanism for
1276 urban and regional scale computer modeling, *J. Geophys. Res.*, 94, 12925-12956, 1989.
- 1277 Ghan, S. J., Leung, L. R., Easter, R. C., Abdul-Razzak, K.: Prediction of cloud droplet number in a
1278 general circulation model, *J. Geophys. Res.*, 102 (D18), 21,777–21,794, 1997.
- 1279 Ghan, S. and Zaveri R.A.: Parameterization of optical properties for hydrated internally mixed aerosol,
1280 *J. Geophys. Res.*, 112, D10201, doi:10.1029/2006JD007927, 2007.
- 1281 Giglio, L., Randerson, J.T., and van der Werf, G.R.: Analysis of daily, monthly, and annual burned
1282 area using the fourth generation Global Fire Emissions Database (GFED4), *J. Geophys. Res.*:
1283 *Biogeosciences*, doi:10.1002/jgrg.20042, 2013.
- 1284 Gong, S. L., X. Zhang, T. Zhao, I. G. Mckendry, D. A. Jaffe, and N. Lu: Characterization of soil dust
1285 aerosol in China and its transport and distribution during 2001 ACE-Asia: 2. Model simulation
1286 and validation, *J. Geophys. Res.*, 108(D9), 4262, doi:10.1029/2002JD002633, 2003.
- 1287 Gong, S.L.: A parameterization of sea-salt aerosol source function for sub- and super-micron particles,
1288 *Global Biogeochem. Cy.*, 17(4), 1097, doi:10.1029/2003GB002079, 2003.
- 1289 Graf, H.-F., Feichter, J., and Langmann, B.: Volcanic sulfur emissions: Estimates of source strength
1290 and its contribution to the global sulfate distribution. *J. Geophys. Res.*, 102(D9), 10727-10738,



- 1291 doi: 10.1029/96JD03265, 1997.
- 1292 Granier, C., Darras, S., Denier van der Gon, H., Doubalova, J., Elguindi, N., Galle, B., Gauss, M.,
1293 Guevara, M., Jalkanen, J.-P., Kuenen, J., Liousse, C., Quack, B., Simpson, D., and Sindelarova,
1294 K.: The Copernicus Atmosphere Monitoring Service global and regional emissions (April 2019
1295 version), Report April 2019 version, doi:10.24380/d0bn-kx16, 2019.
- 1296 Grell, G.A.: Prognostic evaluation of assumptions used by cumulus parameterizations, *Mon. Wea. Rev.*
1297 121, 764-787, 1993.
- 1298 Grell, G.A., Dudhia, J., Stauffer, D.R.: A Description of the Fifth-Generation Penn State/NCAR
1299 Mesoscale Model (MM5), NCAR Technical Note, NCAR/TN-398tSTR, p.117, 1995.
- 1300 Guo, T., Guo, Z., Wang, J., Feng, J., Gao, H., and Yao, X.: Tracer-based investigation of organic
1301 aerosols in marine atmospheres from marginal seas of China to the northwest Pacific Ocean,
1302 *Atmos. Chem. Phys.*, 20, 5055–5070, <https://doi.org/10.5194/acp-20-5055-2020>, 2020.
- 1303 Han, X., Zhang, M. G., Han, Z. W., Xin, J. Y., Liu, X. H.: Simulation of aerosol direct radiative
1304 forcing with RAMS-CMAQ in East Asia, *Atmos. Environ.*, 45, 6576-6592, 2011.
- 1305 Han, Z.: Direct radiative effect of aerosols over East Asia with a regional coupled climate/chemistry
1306 model, *Meteor. Zeit.*, 19, 287–298, 2010.
- 1307 Han, Z. W., Ueda, H., Matsuda, K., Zhang, R. J., Arao, K., Kanai, Y., Hasome, H.: Model study on
1308 particle size segregation and deposition during Asian dust events in March 2002, *J. Geophys.*
1309 *Res.*, 109, D19205, doi:10.1029/2004jd004920, 2004.
- 1310 Han, Z.W., Li, J.W., Xia, X.A., Zhang, R.J.: Investigation of direct radiative effects of aerosols in dust
1311 storm season over East Asia with an online coupled regional climate-chemistry-aerosol model,
1312 *Atmos. Environ.*, 54, 688-699, 2012.
- 1313 Han, Z.W., Li, J.W., Guo, W.D., Xiong, Z., Zhang, W.: A study of dust radiative feedback on dust
1314 cycle and meteorology over East Asia by a coupled regional climate-chemistry-aerosol model,
1315 *Atmos. Environ.*, 68, 54-63, 2013.
- 1316 Han, Z.W., Li, J.W., Yao, X.H., Tan, S.C.: A regional model study of the characteristics and indirect
1317 effects of marine primary organic aerosol in springtime over East Asia, *Atmos. Environ.*, 197,
1318 22–35, 2019.
- 1319 Hsiao, T.-C., Chen, W.-N., Ye, W.-C., Lin, N.-H., Tsay, S.-C., Lin, T.-H., Lee, C.-T., Chuang, M.-T.,
1320 Pantina, P., Wang, S.-H.: Aerosol optical properties at the Lulin Atmospheric Background Station



- 1321 in Taiwan and the influences of long-range transport of air pollutants, *Atmos. Environ.*, 150,
1322 366-378, 2017.
- 1323 Hong, S. H. and Pan, H. L.: Nonlocal boundary layer vertical diffusion in a medium range forecast
1324 model, *Mon. Wea. Rev.*, 124, 2322–2339, 1996.
- 1325 Hoose, C., Kristjánsson, J. E., Iversen T., A. Kirkevåg, Ø. Seland, and Gettelman A.: Constraining
1326 cloud droplet number concentration in GCMs suppresses the aerosol indirect effect, *Geophys.*
1327 *Res. Lett.*, 36, L12807, doi:10.1029/2009GL038568, 2009.
- 1328 Hu, Q.-H., Xie, Z.-Q., Wang, X.-M., Kang, H., He, Q.-F., and Zhang, P.: Secondary organic aerosols
1329 over oceans via oxidation of isoprene and monoterpenes from Arctic to Antarctic, *Sci. Rep.*, 3,
1330 2280, doi:10.1038/srep02280, 2013.
- 1331 Huang, W. T. K., Ickes, L., Tegen, I., Rinaldi, M., Ceburnis, D., and Lohmann, U.: Global relevance of
1332 marine organic aerosol as ice nucleating particles, *Atmos. Chem. Phys.*, 18, 11423–11445,
1333 <https://doi.org/10.5194/acp-18-11423-2018>, 2018.
- 1334 Huff Hartz, K. E., Tischuk, J. E., Chan, M. N., Chan, C. K., Donahue, N. M., and Pandis, S. N.: Cloud
1335 condensation nuclei activation of limited solubility organic aerosol, *Atmospheric Environment* 40,
1336 605–617, 2006.
- 1337 IPCC: Intergovernmental Panel on Climate Change, *Climate Change 2013: The Physical Science*
1338 *Basis. Contribution of Working Group I to the Fifth Assessment Report of the Intergovernmental*
1339 *Panel on Climate Change, Report*, edited by: Stocker, T.F., Qin, D.H., Plattner, G.K., Tignor,
1340 M.M.B., Allen, S. K., Boschung, J., Nauels, A., Xia, Y., Bex, V., and Midgley, P.M., Cambridge
1341 University Press, New York, <http://www.ipcc.ch/report/ar5>, 2013 (last access: 2020/04/30).
- 1342 Jaeglé, L., Quinn, P.K., Bates, T.S., Alexander, B., and Lin, J.T.: Global distribution of sea salt
1343 aerosols: new constraints from in situ and remote sensing observations, *Atmos. Chem. Phys.*, 11,
1344 3137–3157, doi:10.5194/acp-11-3137-2011, 2011.
- 1345 Kanaya, Y., Pan, X., Miyakawa, T., Komazaki, Y., Taketani, F., Uno, I., and Kondo, Y.: Long-term
1346 observations of black carbon mass concentrations at Fukue Island, western Japan, during 2009–
1347 2015: constraining wet removal rates and emission strengths from East Asia, *Atmos. Chem. Phys.*,
1348 16, 10689–10705, <https://doi.org/10.5194/acp-16-10689-2016>, 2016.
- 1349 Kang, M., Fu, P., Kawamura, K., Yang, F., Zhang, H., Zang, Z., Ren, H., Ren, L., Zhao, Y., Sun, Y.,
1350 and Wang, Z.: Characterization of biogenic primary and secondary organic aerosols in the marine



- 1351 atmosphere over the East China Sea, *Atmos. Chem. Phys.*, 18, 13947–13967, 2018.
- 1352 Kelly, J. T., Bhave, P. V., Nolte, C. G., Shankar, U., and Foley, K. M.: Simulating emission and
1353 chemical evolution of coarse sea-salt particles in the Community Multiscale Air Quality (CMAQ)
1354 model. *Geosci. Model Dev.*, 3, 257–273, 2010.
- 1355 Kiehl, J.T., Hack, J.J., Bonan, G.B., Boville, B.A., Briegleb, B.P., Williamson, D.L., Rasch, P.J.:
1356 Description of the NCAR Community Climate Model (CCM3), NCAR Technical Note,
1357 NCAR/TN-420+STR, p.152, 1996.
- 1358 Kunwar, B. and Kawamura, K.: One-year observations of carbonaceous and nitrogenous components
1359 and major ions in the aerosols from subtropical Okinawa Island, an outflow region of Asian dusts,
1360 *Atmos. Chem. Phys.*, 14, 1819–1836, <https://doi.org/10.5194/acp-14-1819-2014>, 2014.
- 1361 Lack, D. A., Tie, X. X., Bofinger, N. D., Wiegand, A. N., and Madronich, S.: Seasonal variability of
1362 secondary organic aerosol: A global modeling study, *J. Geophys. Res.: Atmosphere*, 109, D03203,
1363 doi:10.1029/2003JD003418, 2004.
- 1364 Lee, A., Goldstein, A. H, Kroll, J. H., Ng, N. L., Varutbangkul, V., Flagan, R. C., and Seinfeld, J. H.:
1365 Gas-phase products and secondary aerosol yields from the photooxidation of 16 different
1366 terpenes, *J. Geophys. Res.*, 111, D17305, doi:10.1029/2006JD007050, 2006.
- 1367 Leibensperger, E. M., Mickley, L. J., Jacob, D. J., Chen, W.-T., Seinfeld, J. H., Nenes, A., Adams, P. J.,
1368 Streets, D. G., Kumar, N., and Rind, D.: Climatic effects of 1950–2050 changes in US
1369 anthropogenic aerosols–Part 1: Aerosol trends and radiative forcing, *Atmos. Chem. Phys.*, 12,
1370 3333–3348, 2012.
- 1371 Li, J.-L., Zhang, H.-H., and Yang, G.-P.: Distribution and sea-to-air flux of isoprene in the East China
1372 Sea and the South Yellow Sea during summer, *Chemosphere*, 178, 291-300, 2017.
- 1373 Li, J.-L., Zhai, X., Zhang, H.-H., and Yang, G.-P.: Temporal variations in the distribution and
1374 sea-to-air flux of marine isoprene in the East China Sea, *Atmos. Environ.*, 187, 131–143, 2018.
- 1375 Li, J.W. and Han, Z.W.: A modeling study of the impact of heterogeneous reactions on mineral aerosol
1376 surfaces on tropospheric chemistry over East Asia, *Particuology*, 8, 433-441, 2010.
- 1377 Li, J.W., Han, Z.W., and Zhang, R.J.: Influence of aerosol hygroscopic growth parameterization on
1378 aerosol optical depth and direct radiative forcing over East Asia, *Atmos. Res.*, 140-141, 14-27,
1379 2014.
- 1380 Li, J. W. and Han, Z. W.: Aerosol vertical distribution over east china from RIEMS-Chem simulation



- 1381 in comparison with CALIPSO measurements, *Atmos. Environ.*, 143, 177-189, 2016a.
- 1382 Li, J. W. and Han, Z. W.: Seasonal variation of nitrate concentration and its direct radiative forcing
1383 over East Asia, *Atmosphere*, 7(8), 105, 2016b.
- 1384 Li, J. W., Han, Z. W., Yao, X. H.: A modeling study of the influence of sea salt on inorganic aerosol
1385 concentration, size distribution, and deposition in the western Pacific Ocean, *Atmos. Environ.*,
1386 188, 157-173, 2018.
- 1387 Li, J. W., Han, Z. W., Yao, X. H., Xie, Z. X., Tan, S. C.: The distributions and direct radiative effects
1388 of marine aerosols over East Asia in springtime, *Sci. Tot. Environ.*, 651, 1913–1925, 2019.
- 1389 Li, J., Han, Z., Wu, Y., Xiong, Z., Xia, X., Li, J., Liang, L., and Zhang, R.: Aerosol radiative effects
1390 and feedbacks on boundary layer meteorology and PM_{2.5} chemical components during winter
1391 haze events over the Beijing-Tianjin-Hebei region, *Atmos. Chem. Phys.*, 20, 8659–8690,
1392 <https://doi.org/10.5194/acp-20-8659-2020>, 2020.
- 1393 Li, M., Zhang, Q., Kurokawa, J.-I., Woo, J.-H., He, K., Lu, Z., Ohara, T., Song, Y., Streets, D.G.,
1394 Carmichael, G.R., Cheng, Y., Hong, C., Huo, H., Jiang, X., Kang, S., Liu, F., Su, H., and Zheng,
1395 B.: MIX: a mosaic Asian anthropogenic emission inventory under the international collaboration
1396 framework of the MICS-Asia and HTAP, *Atmos. Chem. Phys.*, 17, 935-963,
1397 [doi:10.5194/acp-17-935-2017](https://doi.org/10.5194/acp-17-935-2017), 2017.
- 1398 Liao, H., Seinfeld, J.H., Adams, P.J., Mickley, L.J.: Global radiative forcing of coupled tropospheric
1399 ozone and aerosols in a unified general circulation model, *J. Geophys. Res.: Atmosphere*, 109,
1400 D16207. <https://doi.org/10.1029/2003JD004456>, 2004.
- 1401 Liu, X. and Wang, J.: How important is organic aerosol hygroscopicity to aerosol indirect forcing?
1402 *Environ. Res. Lett.*, 5(4), 044010, <http://iopscience.iop.org/1748-9326/5/4/044010>, 2010.
- 1403 Lohmann, U. and Feichter J.: Global indirect aerosol effects: a review, *Atmos. Chem. Phys.*, 5, 715–
1404 737, 2005.
- 1405 Long, M. S., Keene, W. C., Kieber, D. J., Erickson, D. J., and Maring, H.: A sea-state based source
1406 function for size- and composition-resolved marine aerosol production, *Atmos. Chem. Phys.*, 11,
1407 1203–1216, <https://doi.org/10.5194/acp-11-1203-2011>, 2011.
- 1408 Luo, G. and Yu, F.: A numerical evaluation of global oceanic emissions of α -pinene and isoprene,
1409 *Atmos. Chem. Phys.*, 10, 2007–2015, [doi:10.5194/acp-10-2007-2010](https://doi.org/10.5194/acp-10-2007-2010), 2010.
- 1410 Luo, L., Yao, X.H., Gao, H.W., Hsu, S.C., Li, J.W., and Kao, S.J.: Nitrogen speciation in various types



- 1411 of aerosols in spring over the northwestern Pacific Ocean, *Atmos. Chem. Phys.*, 16, 325-341,
1412 2016.
- 1413 Luo, L., Kao, S.-J., Bao, H., Xiao, H., Xiao, H., Yao, X., Gao, H., Li, J., and Lu, Y.: Sources of
1414 reactive nitrogen in marine aerosol over the Northwest Pacific Ocean in spring, *Atmos. Chem.*
1415 *Phys.*, 18, 6207–6222, 2018.
- 1416 Ma, Q. X., Wu, Y. F., Zhang, D. Z., Wang, X. J., Xia, Y. J., Liu, X. Y., Tian, P., Han, Z. W., Xia, X. A.,
1417 Wang, Y., and Zhang, R. J.: Roles of regional transport and heterogeneous reactions in the PM_{2.5}
1418 increase during winter haze episodes in Beijing, *Sci. Total. Environ.*, 599/600, 246–253, 2017.
- 1419 Martin, G. M., Johnson, D. W., and Spice, A.: The Measurements and Parameterization of Effective
1420 Radius of Droplets in Warm Stratocumulus Clouds, *J. Atmos. Sci.*, 51, 1823–1842, 1994.
- 1421 Meskhidze, N. and Nenes, A.: Phytoplankton and cloudiness in the Southern Ocean, *Science*, 314,
1422 1419–1423, 2006.
- 1423 Meskhidze, N., Xu, J., Gantt, B., Zhang, Y., Nenes, A., Ghan, S.J., Liu, X., Easter, R., Zaveri, R.:
1424 Global distribution and climate forcing of marine organic aerosol: 1. Model improvements and
1425 evaluation, *Atmos. Chem. Phys.*, 11, 11689–11705, 2011.
- 1426 Miyazaki Yuzo, Kawamura Kimitaka, and Sawano Maki: Size distributions and chemical
1427 characterization of water-soluble organic aerosols over the western North Pacific in summer, *J.*
1428 *Geophys. Res.*, 115, D23210, doi:10.1029/2010JD014439, 2010.
- 1429 Monahan, E. C., Spiel, D. E., Davidson, K. L.: A model of marine aerosol generation via white caps
1430 and wave disruption. In: *Oceanic Whitecaps*. D. Reidel, Norwell, Mass, pp. 167–174, 1986.
- 1431 Myriokefalitakis, S., Vignati, E., Tsigaridis, K., Papadimas, C., Sciare, J., Mihalopoulos, N., Facchini,
1432 M.C., Rinaldi, M., Dentener, F.J., Ceburnis, D., Hatzianastasiou, N., O’Dowd, C.D., van Weele,
1433 M., and Kanakidou, M.: Global modeling of the oceanic source of organic aerosols. *Adv. Meteor.*,
1434 939171, doi:10.1155/2010/939171, 2010.
- 1435 NOAA/NCEP: NCEP FNL Operational Model Global Tropospheric Analyses, continuing from July
1436 1999. Research Data Archive at the National Center for Atmospheric Research, Computational
1437 and Information Systems Laboratory. Dataset. <https://doi.org/10.5065/D6M043C6>, 2000, Last
1438 accessed, 2019/12/12.
- 1439 OBPG: NASA Goddard Space Flight Center, Ocean Ecology Laboratory, Ocean Biology Processing
1440 Group: Visible and Infrared Imager/Radiometer Suite (VIIRS) Chlorophyll Data; NASA



- 1441 OB.DAAC, Greenbelt, MD, USA. doi:10.5067/NPP/VIIRS/L3M/CHL/2018.
- 1442 O'Dowd, C.D., Facchini, M.C., Cavalli, F., Ceburnis, D., Mircea, M., Decesari, S., Fuzzi, S., Yoon,
1443 Y.J., Putaud, J.P.: Biogenically driven organic contribution to marine aerosol, *Nature*, 431, 676–
1444 680, 2004.
- 1445 Ovadnevaite, J., Ceburnis, D., Martucci, G., Bialek, J., Monahan, C., Rinaldi, M., Facchini, M.C.,
1446 Berresheim, H., Worsnop, D.R., O'Dowd, C.: Primary marine organic aerosol: a dichotomy of
1447 low hygroscopicity and high CCN activity, *Geophys. Res. Lett.*, 38, L21806.
1448 <https://doi.org/10.1029/2011GL048869>, 2011.
- 1449 Petters, M.D. and Kreidenweis, S.M.: A single parameter representation of hygroscopic growth and
1450 cloud condensation nucleus activity, *Atmos. Chem. Phys.*, 7, 1961-1971, 2007.
- 1451 Quinn, P. K., Bates Timothy S., Schulz Kristen S., Coffman D. J., Frossard A. A., Russell L. M.,
1452 Keene W. C. and Kieber D. J.. Contribution of sea surface carbon pool to organic matter
1453 enrichment in sea spray aerosol. *Nat. Geosci.* 7, 228-232, 2014.
- 1454 Quinn, P. K., Coffman, D. J., Johnson, J. E., Upchurch, L. M., and Bates, T. S.: Small fraction of
1455 marine cloud condensation nuclei made up of sea spray aerosol, *Nat. Geosci.*, 10, 674–679, 2017.
- 1456 Rap, A., Scott, C.E., Spracklen, D.V., Bellouin, N., Forster, P.M., Carslaw, K.S., Schmidt, A., and
1457 Mann, G.: Natural aerosol direct and indirect radiative effects, *Geophys. Res. Lett.*, 40,
1458 3297-3301, doi:10.1002/grl.50441, 2013.
- 1459 Reisner, J., Rasmussen, R.M., Bruintjies, R.T.: Explicit forecasting of super cooled liquid water in
1460 winter storms using the MM5 mesoscale model, *Quart. J. Roy. Meteor. Soc.*, 124 (548), 1071–
1461 1107, 1998.
- 1462 Riemer, N., West, M., Zaveri, R., Easter, R.: Estimating black carbon aging time-scales with a
1463 particle-resolved aerosol model, *J. Aerosol Sci.*, 41, 143-158, 2010.
- 1464 Roelofs, G.J.: A GCM study of organic matter in marine aerosol and its potential contribution to cloud
1465 drop activation, *Atmos. Chem. Phys.*, 8, 709–719 2008, 2008.
- 1466 Sayer, A. M., Hsu, N. C., Bettenhausen, C., Lee, J., Kim, W. V., and Smirnov, A.: Satellite Ocean
1467 Aerosol Retrieval (SOAR) Algorithm Extension to S-NPP VIIRS as Part of the “Deep Blue”
1468 Aerosol Project, *J. Geophys. Res. Atmos.*, 123, doi:10.1002/2017JD027412, 2018.
- 1469 Shao, Y. and Dong, C.H.: A review on East Asian dust storm climate, modeling and monitoring, *Glob.*
1470 *Planet. Change*, 52, 1-22, 2006.



- 1471 Sindelarova, K., Granier, C., Bouarar, I., Guenther, A., Tilmes, S., Stavrou, T., Müller, J.-F., Kuhn,
1472 U., Stefani, P., and Knorr, W.: Global data set of biogenic VOC emissions calculated by the
1473 MEGAN model over the last 30 years. *Atmos. Chem. Phys.*, 14, 9317–9341.
1474 <https://doi.org/10.5194/acp-14-9317-2014>, 2014.
- 1475 Slingo A.: A GCM Parameterization for the Shortwave Radiative Properties of Water Clouds, *J. Atmos.*
1476 *Sci.*, 46(10), 1419-1427, 1989.
- 1477 Slinn, W. G. N.: Precipitation scavenging: in *Atmospheric Science and Power Production*. pp. 466–
1478 532, Technical Information Center, Office of Science and Technology Information, Department
1479 of Energy, Washington, D. C., 1984.
- 1480 Smith, S.J., van Aardenne, J., Klimont, Z., Andres, R.J., Volke, A., and Delgado Arias, S.:
1481 Anthropogenic sulfur dioxide emissions: 1850-2005, *Atmos. Chem. Phys.*, 11, 1101-1116, 2011.
- 1482 Spracklen, D.V., Arnold, S.R., Carslaw, K.S., Sciare, J., and Pio, C.: Globally significant oceanic
1483 source of organic carbon aerosol, *Geophys. Res. Lett.*, 35, L12811, doi:10.1029/2008GL033359,
1484 2008.
- 1485 Surratt, J. D., Chan, A. W. H., Eddingsaas, N. C., Chan, M. N., Loza, C. L., Kwan, A. J., Hersey, S. P.,
1486 Flagan, R. C., Wennberg, P. O., and Seinfeld, J. H.: Reactive intermediates revealed in secondary
1487 organic aerosol formation from isoprene, *P. Natl. Acad. Sci. USA*, 107, 6640–6645,
1488 doi:10.1073/pnas.0911114107, 2010.
- 1489 Tan, S. C., Li, J. W., Che, H. Z., Chen, B., and Wang, H.: Transport of East Asian dust storms to the
1490 marginal seas of China and the southern North Pacific in spring 2010, *Atmos. Environ.*, 148,
1491 316-328, 2017.
- 1492 Tao, J., Surapipith, V., Han, Z. W., Prapamontol, T., Kawichai, S., Zhang, L. M., Zhang, Z. S., Wu, Y.
1493 F., Li, J. W., Li J., Yang, Y. H., and Zhang, R. J.: High mass absorption efficiency of
1494 carbonaceous aerosols during the biomass burning season in Chiang Mai of northern Thailand,
1495 *Atmos. Environ.*, 240, 117821, 2020.
- 1496 Van den Berg, A., Dentener, F., and Lelieveld, J.: Modeling the chemistry of the marine boundary
1497 layer: Sulphate formation and the role of sea-salt aerosol particles, *J. Geophys. Res.*, 105, 11671–
1498 11698. <https://doi.org/10.1029/1999JD901073>, 2000.
- 1499 Vignati, E., Facchini, M.C., Rinaldi, M., Scannell, C., Ceburnis, D., Sciare, J., Kanakidou, M.,
1500 Myriokefalitakis, S., Dentener, F., and O’Dowd, C.D.: Global scale emission and distribution of



- 1501 seaspray aerosol: sea-salt and organic enrichment, *Atmos. Environ.*, 44, 670–677, 2010.
- 1502 Xiong, Z., Fu, C. B., and Yan, X. D.: Regional Integrated environmental model system and its
1503 simulation of East Asia summer monsoon, *Chinese Sci. Bull.*, 54(22), 4253-4261, 2009.
- 1504 Wang, F. W., Guo, Z. G., Lin, T., Hu, L. M., Chen, Y. J., and Zhu, Y. F.: Characterization of
1505 carbonaceous aerosols over the East China Sea: The impact of the East Asian continental outflow,
1506 *Atmos. Environ.*, 110, 163-173, 2015.
- 1507 Wang, M., and Penner J. E.: Aerosol indirect forcing in a global model with particle nucleation, *Atmos.*
1508 *Chem. Phys.*, 9, 239– 260, 2009.
- 1509 Wang, S. Y., Fu, C. B., Wei, H. L., Qian, Y., Xiong, Z., Feng, J. M., Zhao, D. M., Dan, L., Han, Z. W.,
1510 Su, B. K., Zhao, M., Zhang, Y. C., Tang, J. P., Liu, H. N., Wu, J., Zeng, X. M., Chen, M., Wang,
1511 L. Z.: Regional integrated environmental modeling system: development and application,
1512 *Climatic Change*, 129, 499-510, 2015.
- 1513 Westervelt, D. M., Moore, R. H., Nenes, A., and Adams, P. J.: Effect of primary organic sea spray
1514 emissions on cloud condensation nuclei concentrations, *Atmos. Chem. Phys.*, 12, 89–101.
1515 <https://doi.org/10.5194/acp-12-89-2012>, 2012.
- 1516 Wu, Y. F., Wang, X. J., Tao, J., Huang, R. J., Tian, P., Cao, J. J., Zhang, L. M., Ho, K. F., Han, Z. W.,
1517 Zhang, R. J.: Size distribution and source of black carbon aerosol in urban Beijing during winter
1518 haze episodes, *Atmos. Chem. Phys.*, 17, 7965-7975, 2017.
- 1519 Zeng, S., Riedi, J., Trepte, C. R., Winker, D. M. & Hu, Y. X.: Study of global cloud droplet number
1520 concentration with A-Train satellites. *Atmos. Chem. Phys.* 14, 7125–7134, 2014.
- 1521 Zhang, K. M., Knipping, E. M., Wexler, A. S., Bhave, P. V., and Tonnesen, G. S.: Size distribution of
1522 sea-salt emissions as a function of relative humidity, *Atmos. Environ.*, 39, 3373-3379, 2005.
- 1523 Zhang, L. M., Gong, S. L., Padro, J., and Barrie, L.: A size-segregated particle dry deposition scheme
1524 for an atmospheric aerosol module, *Atmos. Environ.*, 35(3), 549-560, 2001.
- 1525 Zhao, B., Liou, K. N., Gu, Y., Li, Q., Jiang, J. H., Su, H., He, C., Tseng, H. R., Wang, S., Liu, R., Qi,
1526 L., Lee, W. L., and Hao, J.: Enhanced PM_{2.5} pollution in China due to aerosol-cloud interactions,
1527 *Sci. Rep.*, 7, 4453, <https://doi.org/10.1038/s41598-017-04096-8>, 2017.
- 1528 Zhu, C., Kawamura, K., and Fu, P.: Seasonal variations of biogenic secondary organic aerosol tracers
1529 in Cape Hedo, Okinawa, *Atmos. Environ.*, 130, 113-119, 2016.
- 1530

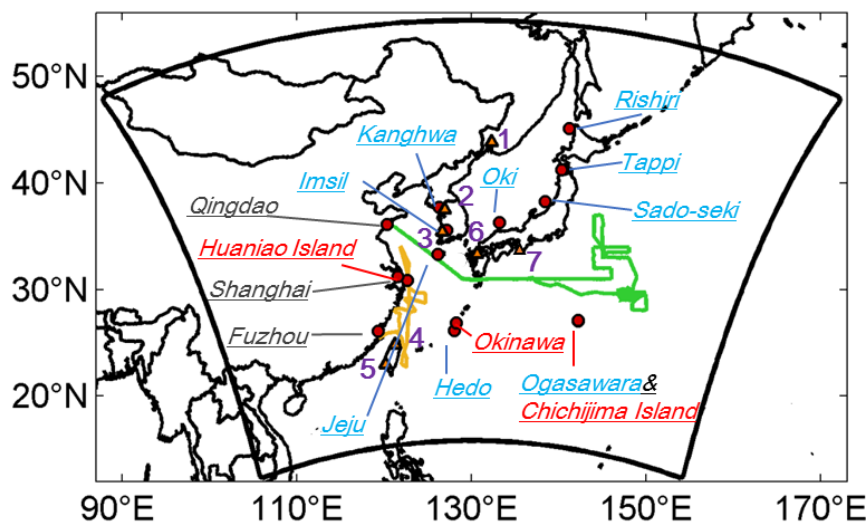


Figure 1. Model domain, observational sites, and research cruise tracks. EANET sites are marked in light-blue. Observation sites of carbonaceous aerosols are marked in red (Chichijima Island: Boreddy et al., 2018; Fukue: Kanaya et al., 2016; Okinawa: Kunwar and Kawamura, 2014; Huaniao Island: Wang F. W. et al., 2014). Three CNEMC sites are marked in grey (Qingdao, Shanghai, and Fuzhou). Two research cruise tracks are represented by green line (Dongfanghong II from 17 March to 22 April 2014: Luo et al., 2016; Feng et al., 2017) and orange line (KEXUE-1 from 18 May to 12 June 2014: Kang et al., 2018), respectively. AERONET sites are represented by triangles with numbers (1-Ussuriysk, 2-Yonsei_University, 3-Gwangju_GIST, 4-EPA-NCU, 5-Chen-Kung_Univ, 6-Fukuoka, and 7-Shirahama). Full names of abbreviations are given in the text.

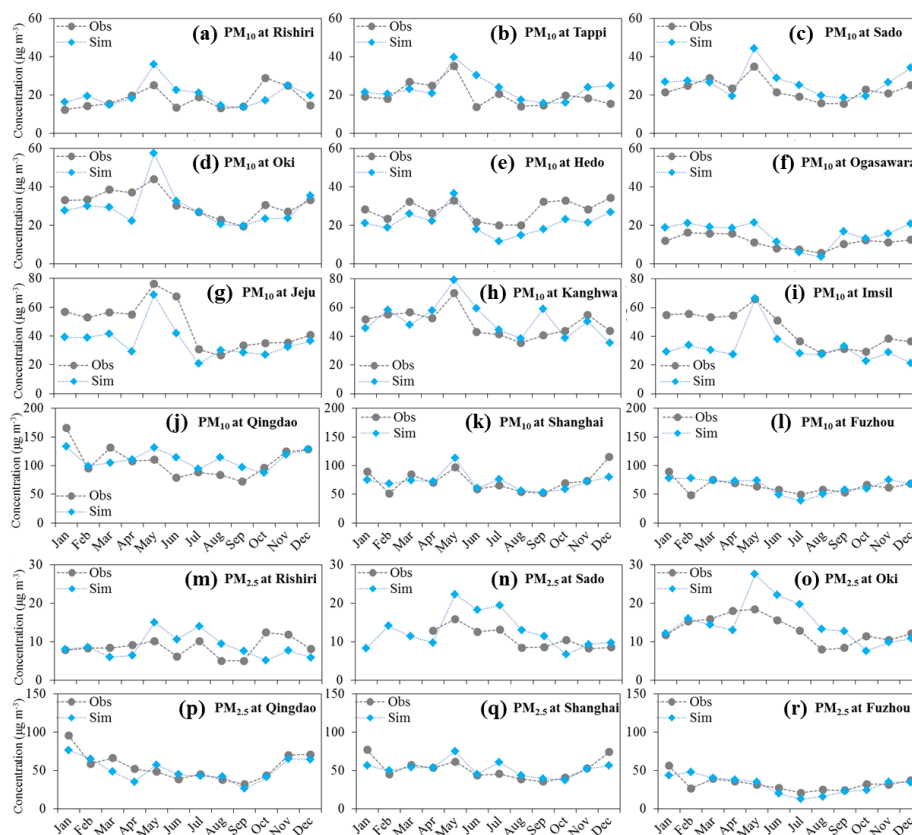


Figure 2. The model simulated (Sim) and observed (Obs) monthly PM_{10} (a–l) and $PM_{2.5}$ (m–r) concentrations at EANET and CNEMC sites for the year 2014. The monthly data were averaged from hourly observations and the simulations were sampled according to the observations.

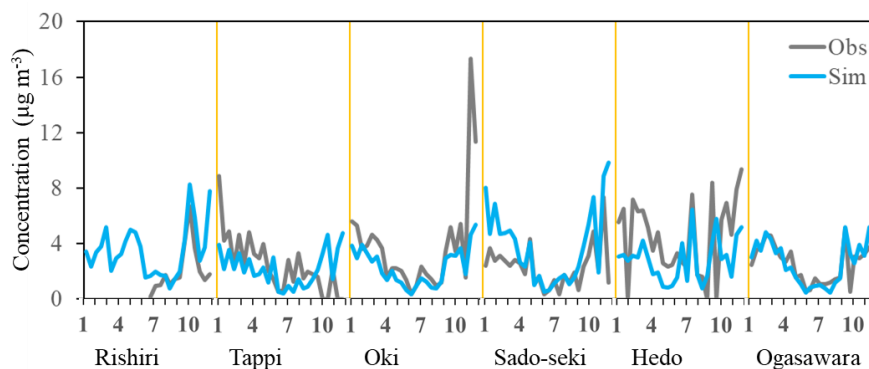


Figure 3. Observed and model simulated sodium (Na^+) concentrations (bi-weekly samples) at 6 coastal/island EANET sites in Japan for the year 2014. The x axis is month for each site.

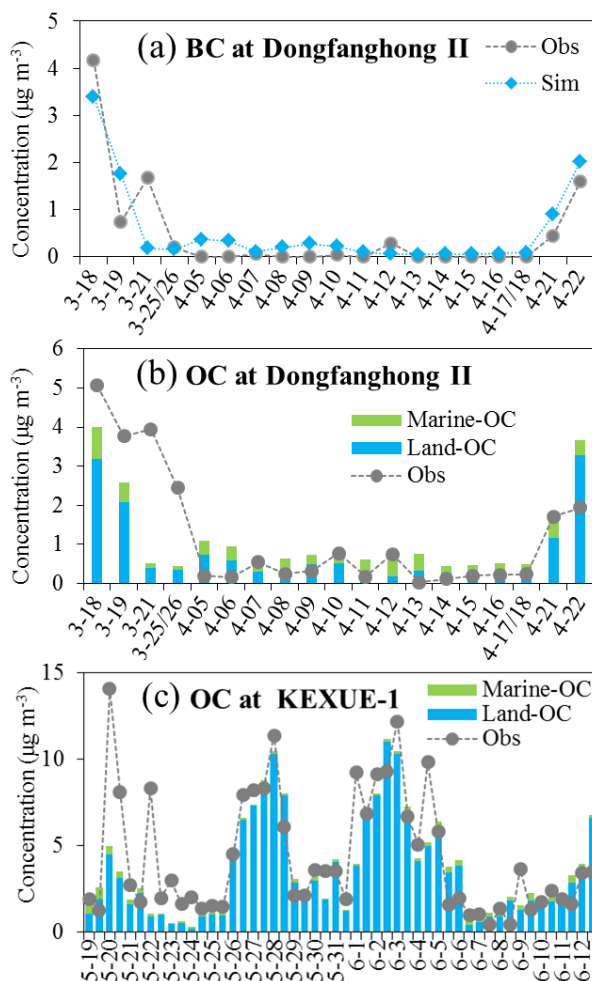


Figure 4. The model simulated (bars) and observed (dotted lines) daily BC and OC concentrations from the spring campaign (a, b) and half-day OC concentrations from the early summer campaign (c). The modeled total OC concentration was decomposed into those from marine (green bars) and land (blue bars) sources.

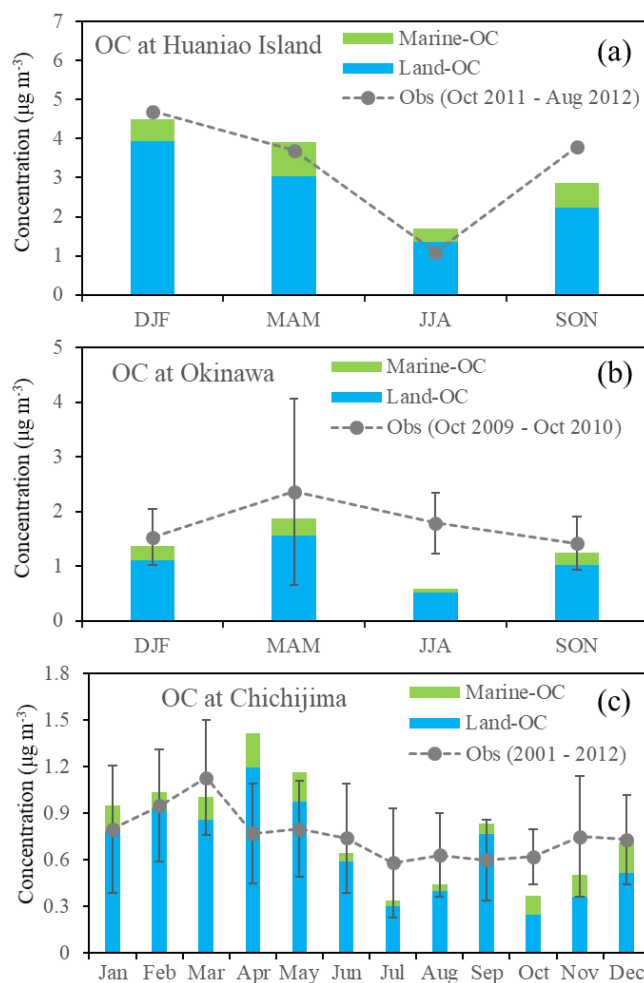


Figure 5. The model simulated (bars) and observed (dotted lines) OC concentrations at different sites. Seasonal mean concentrations were provided at (a) Huaniao Island (Wang et al., 2015) and (b) Okinawa (Kunwar and Kawamura, 2014) while monthly mean concentrations were provided at (c) Chichijima Island (Boreddy et al., 2018). Standard deviations were available at Okinawa and Chichijima. The modeled OC concentrations were decomposed to marine (green bars) and land (blue bars) sources. The simulation is for the year 2014.

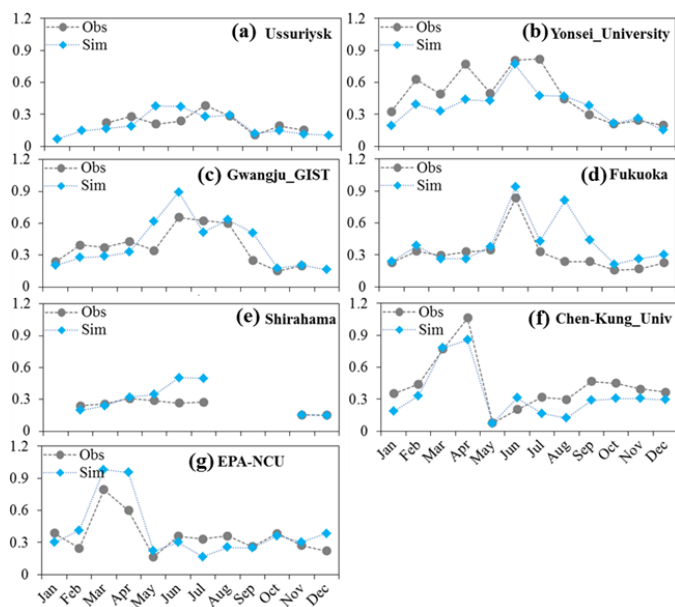


Figure 6. The model simulated (Sim) and observed (Obs) monthly mean AOD at 7 AERONET sites for the year 2014. The monthly mean observations were calculated from hourly data and the corresponding simulations were sampled according to the observations.

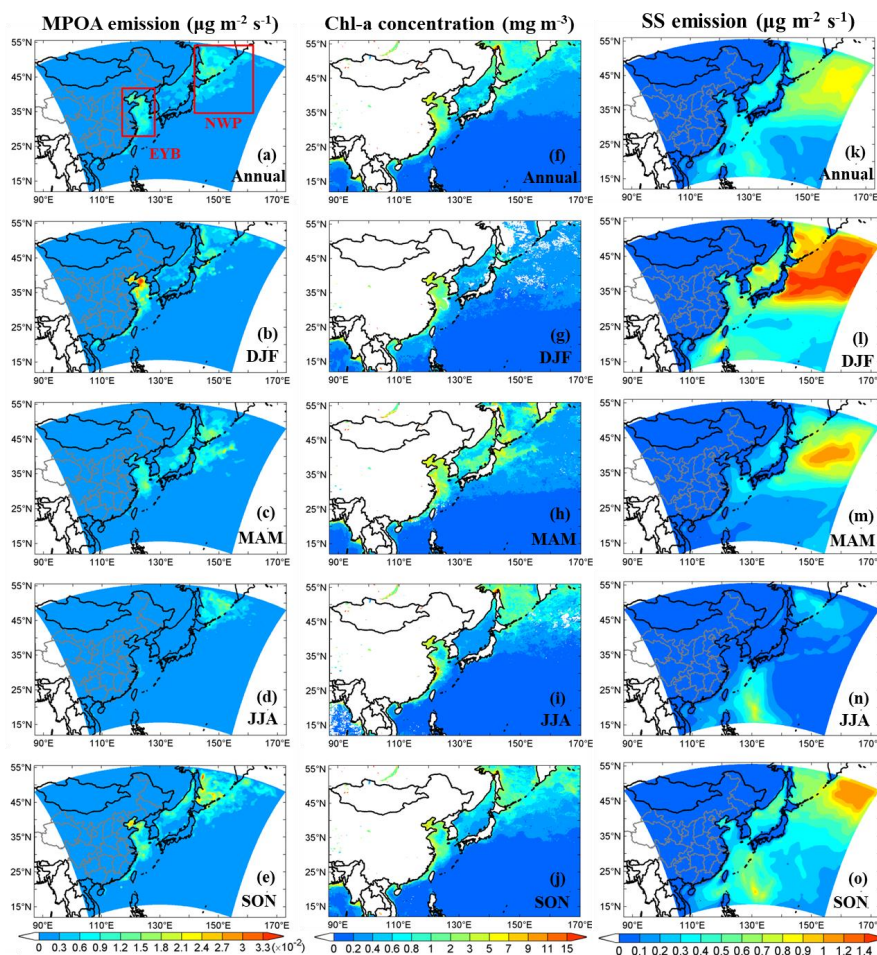


Figure 7. Model simulated annual and seasonal mean distributions of MPOA emissions (a~e), VIIRS retrieved surface sea water chlorophyll-a (Chl-a) concentrations (f~j), and model simulated sea salt (SS) emissions (k~o). Two hotspot regions are marked with red boxes: the region including the East China Sea, the Yellow Sea, and the Bohai Sea (EYB, 27~40°N, 115~123°E) and the region including the northern parts of the western Pacific to the northeast of Japan (NWP, 35~55°N, 140~160°E). Units are given in parentheses.

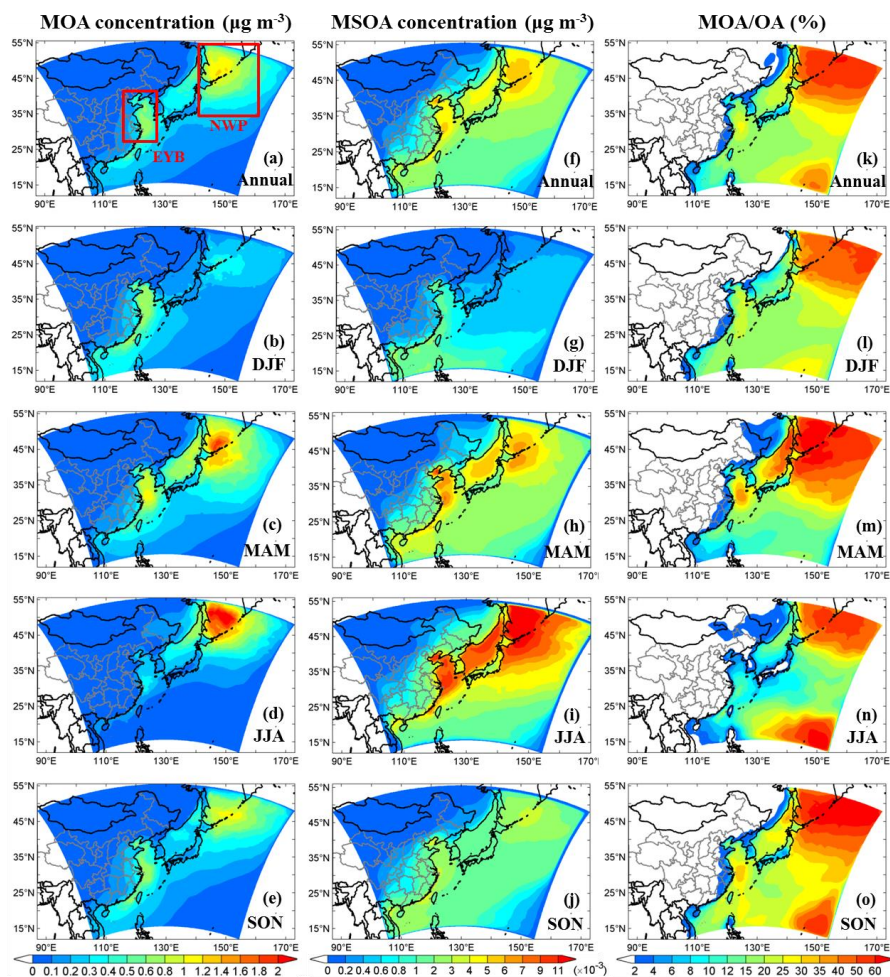


Figure 8. Model simulated annual and seasonal mean near surface MOA (primary+secondary) concentrations (a~e), near surface MSOA concentrations (f~j), and percentage contributions of MOA to total OA (k~o). The two regions of the EYB (27~40°N, 115~123°E) and the NWP (35~55°N, 140~160°E) are marked in 8a. Units are given in parentheses.

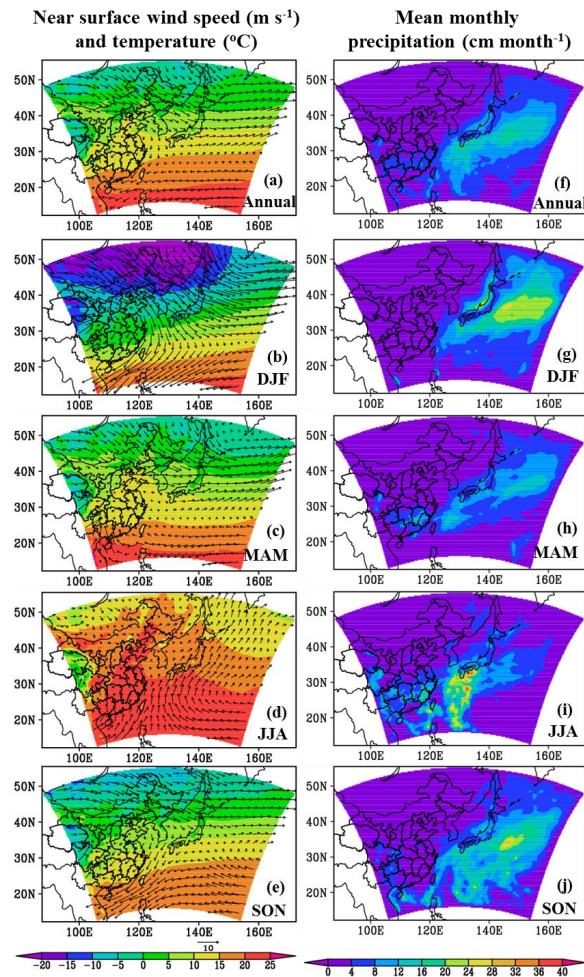


Figure 9. Model simulated annual and seasonal mean near surface temperatures (unit: °C) overlaid with wind vectors (unit: m s⁻¹) (a~e) and mean monthly precipitations (unit: cm month⁻¹) (f~j).

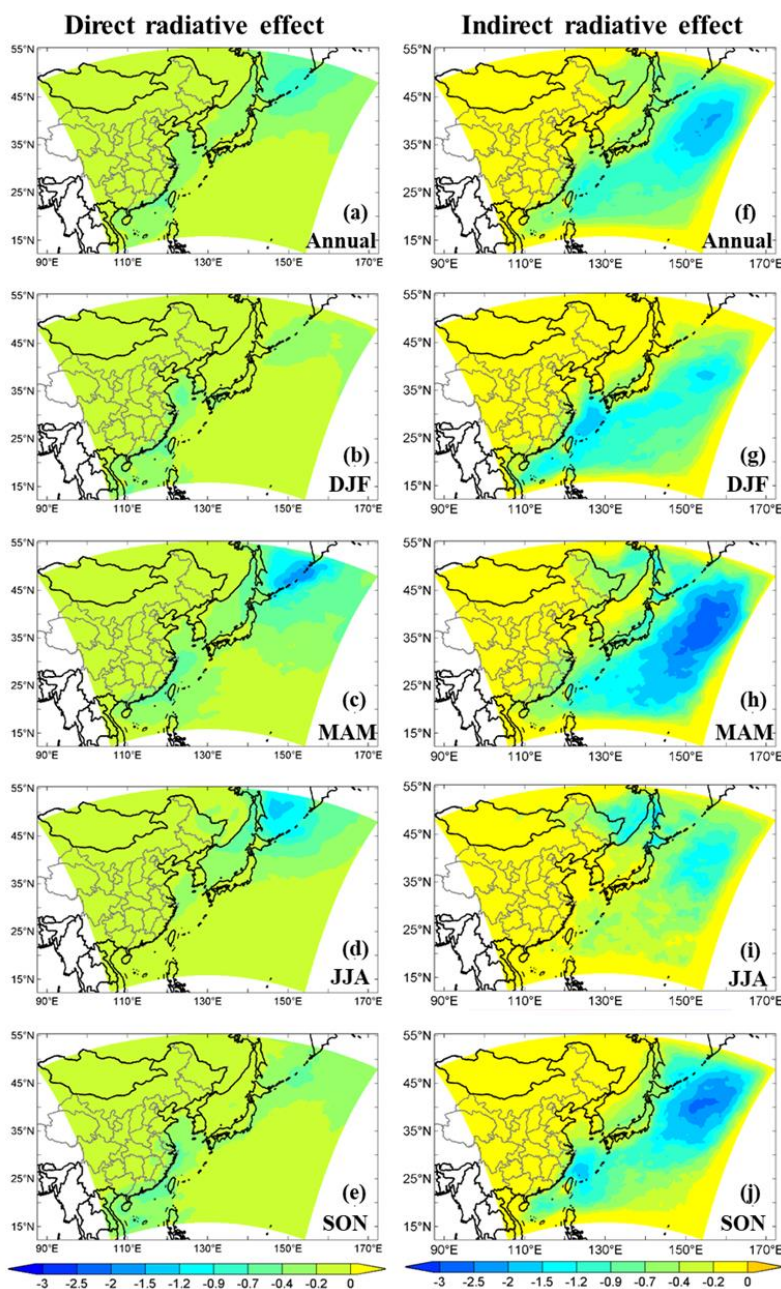


Figure 10. Model simulated annual and seasonal mean direct radiative effect due to MOA (DRE_{MOA}) (a~e) and indirect radiative effect due to MOA (IRE_{MOA}) (f~j) at the top of atmosphere (TOA) under all-sky condition (unit: $W m^{-2}$).

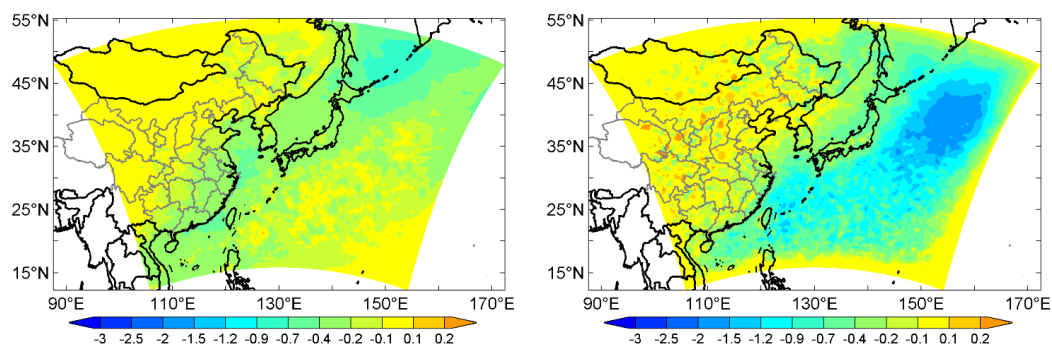


Figure 11. Model simulated annual mean (a) direct radiative effect of MOA due to aerosol-radiation interaction, (b) indirect radiative effect of MOA due to aerosol-cloud interaction at the top of atmosphere (TOA) (unit: W m^{-2})



Table 1. Annual and seasonal performance statistics for hourly PM₁₀ and PM_{2.5} concentrations (unit: $\mu\text{g m}^{-3}$) at EANET sites for the year 2014. Mean observation (Obs), mean simulation (Sim), correlation coefficient (R), and normalized mean bias (NMB in %) are listed. ANN=annual, DJF=December-January-February, MAM=March-April-May, JJA=June-July-August, and SON=September-October-November.

Sites	Samples	ANN			DJF			MAM			JJA			SON								
		Obs	Sim	R	NMB	Obs	Sim	R	NMB	Obs	Sim	R	NMB	Obs	Sim	R	NMB					
PM₁₀																						
Rishiri	8381	18.0	19.9	0.53	11	13.6	18.4	0.65	35	20.1	23.0	0.56	15	15.2	19.4	0.42	28	23.0	18.8	0.51	-18	
Tappi	8584	20.1	23.2	0.49	15	17.4	22.3	0.54	28	29.0	28.0	0.59	-4	16.1	23.8	0.18	48	17.6	18.5	0.39	5	
Sado	8640	22.8	26.4	0.63	16	23.6	29.5	0.68	25	29.2	30.3	0.65	4	18.6	24.5	0.55	32	19.6	21.4	0.53	9	
OkI	8424	31.3	29.2	0.68	-7	33.2	31.1	0.65	-7	40.2	37.5	0.71	-7	26.7	26.6	0.61	0	25.8	22.3	0.66	-14	
Hedo	8008	27.7	21.7	0.56	-22	28.8	22.4	0.66	-22	30.5	28.3	0.58	-7	20.7	14.8	0.54	-28	30.9	20.8	0.34	-33	
Ogasawara	8120	11.5	15.7	0.48	36	13.4	20.3	0.38	52	14.2	19.7	0.40	39	7.0	6.8	0.46	-2	11.2	15.0	0.30	34	
Jeju	7101	46.9	36.9	0.64	-21	50.1	38.2	0.71	-24	62.6	46.6	0.66	-26	36.4	31.5	0.44	-13	34.7	29.3	0.44	-15	
Kanghwa	8524	49.2	51.2	0.59	4	50.2	46.0	0.60	-8	59.9	61.9	0.66	3	40.0	47.2	0.47	18	46.5	49.3	0.38	6	
Imsil	8383	44.5	32.3	0.58	-27	48.8	27.9	0.63	-43	58.0	42.1	0.62	-27	38.4	31.1	0.47	-19	33.0	28.2	0.42	-15	
Average	74165	30.0	28.5	0.65	-5	30.8	28.3	0.67	-8	37.9	35.2	0.65	-7	23.9	25.1	0.59	5	26.9	25.0	0.58	-7	
PM_{2.5}																						
Rishiri	8331	8.6	8.7	0.54	0																	
Sado	6517	11.0	13.4	0.53	21	8.1	7.4	0.78	-8	9.2	9.2	0.56	0	7.2	11.5	0.54	59	10.0	6.7	0.31	-33	
OkI	8410	13.1	15.0	0.64	14	8.5	9.8	0.60	14	14.4	16.1	0.63	12	11.4	16.8	0.47	48	9.1	9.1	0.24	0	
Average	23258	10.9	12.3	0.61	12	13.0	12.9	0.77	-1	17.4	18.7	0.64	8	12.1	18.3	0.55	51	10.1	10.0	0.39	-1	



Table 2. Same as Table 1 but for CNEMC sites.

Sites	Samples	ANN			DJF			MAM			JJA			SON							
		Obs	Sim	R	NMB	Obs	Sim	R	NMB	Obs	Sim	R	NMB	Obs	Sim	R	NMB				
PM₁₀																					
Qingdao	7622	107.0	108.6	0.61	1	131.0	124.3	0.76	-5	117.3	109.9	0.49	-6	83.6	108.4	0.64	30	97.1	101.4	0.59	4
Shanghai	7581	73.4	70.5	0.55	-4	93.9	81.1	0.72	-14	83.2	80.2	0.58	-4	59.6	64.0	0.37	7	64.8	60.6	0.43	-7
Fuzhou	7610	63.7	63.8	0.38	0	69.9	72.9	0.30	4	69.8	72.6	0.32	4	55.3	45.8	0.28	-17	60.5	64.5	0.30	7
Average	22813	81.6	80.7	0.65	-1	98.4	92.6	0.74	-6	89.9	86.7	0.58	-4	66.0	72.0	0.61	9	74.1	75.4	0.51	2
PM_{2.5}																					
Qingdao	7627	55.2	48.7	0.72	-12	75.1	67.8	0.83	-10	56.3	43.7	0.61	-22	40.5	42.8	0.60	6	48.2	43.9	0.74	-9
Shanghai	7724	51.9	51.8	0.62	0	68.0	59.6	0.80	-12	57.2	57.5	0.60	0	42.6	49.8	0.46	17	42.6	42.9	0.51	1
Fuzhou	7641	32.3	30.0	0.44	-7	40.3	40.2	0.25	0	35.8	36.8	0.37	3	24.0	15.8	0.38	-34	29.2	27.3	0.29	-7
Average	22992	46.6	43.4	0.70	-7	61.1	55.8	0.78	-9	49.7	45.6	0.63	-8	35.6	35.5	0.62	0	39.9	38.0	0.62	-5



Table 3. Performance statistics for BC and OC from the two research campaigns in 2014. BC and OC were measured on Dongfanghong II during the spring campaign whereas only OC were collected on KEXUE-1 during the early summer campaign. Mean observation (Obs), mean simulation (Sim), correlation coefficient (R), and normalized mean bias (NMB in %) are listed. The modeled concentrations of marine-OC (including MPOA and MSOA) and its contribution to total OC were estimated.

	Dongfanghong II			KEXUE-1	
	BC	OC	Marine-OC (% in OC)	OC	Marine-OC (% in OC)
Samples	19	19		51	
Obs ($\mu\text{g m}^{-3}$)	0.49	1.20		4.26	
Sim ($\mu\text{g m}^{-3}$)	0.55	1.14	0.33 (29%)	3.68	0.23 (6%)
R	0.87	0.66		0.75	
NMB (%)	13	-5		-13	



Table 4. Comparison of model simulated and observed seasonal OC concentrations (unit: $\mu\text{g m}^{-3}$) at Huaniao Island and Okinawa. The modeled concentrations of marine-OC and its contribution to total OC were estimated. ANN=annual, DJF=December-January-February, MAM=March-April-May, JJA=June-July-August, and SON=September-October-November.

		Time	ANN ^c	DJF	MAM	JJA	SON	Reference
OC								
Huaniao Island	Obs	Oct 2011~ Aug 2012	3.3	4.7	3.7	1.1	3.8	Wang F. W. et al., 2015
	Sim	2014	3.2	4.5	3.9	1.7	2.9	
	Marine-OC		0.6	0.56	0.88	0.32	0.65	
	(% in OC)		(19%)	(12%)	(22%)	(19%)	(23%)	
Okinawa	Obs	Oct 2009~ Oct 2010	1.8	1.5	2.4	1.8	1.4	Kunwar and Kawamura, 2014
	Sim	2014	1.3	1.4	1.9	0.6	1.2	
	Marine-OC		0.21	0.25	0.32	0.06	0.23	
	(% in OC)		(17%)	(18%)	(17%)	(10%)	(18%)	

a: The location of Huaniao Island is 30.86°N, 122.67°E.

b: The location of Okinawa Island is 26.15°N, 128.03°E.

c: The annual means are averages of the four seasonal means.



Table 5. Comparison of model simulated and observed monthly mean OC concentrations (unit: $\mu\text{g m}^{-3}$) at Chichijima Island. Marine-OC concentration and its contribution to total OC were estimated.

Month	Jan	Feb	Mar	Apr	May	Jun	Jul	Aug	Sep	Oct	Nov	Dec	Annual
Obs ^a	0.80	0.95	1.13	0.77	0.80	0.74	0.58	0.63	0.60	0.62	0.75	0.73	0.76
Sim ^b	0.95	1.03	1.01	1.42	1.17	0.64	0.34	0.44	0.84	0.37	0.50	0.71	0.78
Marine-OC	0.17	0.11	0.15	0.22	0.19	0.06	0.04	0.04	0.07	0.12	0.14	0.19	0.13
(% in OC)	(18%)	(11%)	(15%)	(16%)	(16%)	(9%)	(11%)	(9%)	(8%)	(33%)	(28%)	(27%)	(16%)

a: Observations at Chichijima Island (27.07°N, 142.22°E) were obtained from Boreddy et al. (2018) and are 12-yr averages (2001-2012).

b: Simulations are for the year 2014.



Table 6. Performance statistics for hourly AOD (unitless) at AERONET sites for the year 2014. Mean observation (Obs), mean simulation (Sim), correlation coefficient (R), and normalized mean bias (NMB in %) are listed. IDs are marked in Figure 1.

ID	Site	Obs	Sim	R	NMB	Samples
1	Ussuriysk	0.22	0.21	0.41	-6	945
2	Yonsei_University	0.48	0.37	0.67	-23	1629
3	Gwangju_GIST	0.33	0.36	0.53	7	900
4	EPA-NCU	0.38	0.39	0.43	4	685
5	Chen-Kung_ Univ	0.49	0.37	0.60	-25	657
6	Fukuoka	0.28	0.34	0.50	18	1144
7	Shirahama	0.26	0.31	0.40	19	752
	Average	0.36	0.34	0.54	-6	6712

Table 7. Modeled domain and annual/seasonal mean MPOA emission rates, surface sea water chlorophyll-a (Chl-a) concentrations, and sea salt emission fluxes over the western Pacific of East Asia (Mean), the region including the East China Sea, the Yellow Sea, and the Bohai Sea (EYB) and the region including northern parts of western Pacific to the northeast of Japan (NWP).

	MPOA emission ($\times 10^{-2} \mu\text{g m}^{-2} \text{s}^{-1}$)				Chl-a concentration (mg m^{-3})			Sea salt emission flux ($\mu\text{g m}^{-2} \text{s}^{-1}$)		
	Mean ^a	Max ^b	EYB ^c	NWP ^d	Mean ^a	EYB ^c	NWP ^d	Mean ^a	EYB ^c	NWP ^d
ANN	0.16	1.8	0.65	0.40	1.17	3.51	0.96	0.36	0.18	0.59
DJF	0.18	3.6	1.19	0.33	0.67	3.20	0.37	0.63	0.35	1.09
MAM	0.17	2.5	0.41	0.43	0.97	4.00	1.13	0.30	0.11	0.61
JJA	0.08	1.9	0.12	0.29	1.07	3.14	0.90	0.14	0.04	0.15
SON	0.20	3.5	0.88	0.54	1.10	2.90	0.90	0.38	0.24	0.53

a: Mean over oceanic areas.

b: Maximums over oceanic areas.

c: Ocean areas within 27~40°N, 115~123°E.

d: Ocean areas within 35~55°N, 140~160°E.



Table 8. Modeled domain and annual/seasonal mean near surface MOA concentrations, MSOA concentrations, and MOA to total OA ratios over the western Pacific of East Asia (Mean), the EYB region, and the NWP region.

	MOA concentration ($\mu\text{g m}^{-3}$)				MSOA concentration ($\times 10^{-3} \mu\text{g m}^{-3}$)				MOA/OA (%)			
	Mean ^a	Max ^b	EYB ^c	NWP ^d	Mean ^a	Max ^b	EYB ^c	NWP ^d	Mean ^a	Max ^b	EYB ^c	NWP ^d
ANN	0.27	1.2	0.48	0.59	2.2	6.9	4.1	3.8	26%	62%	13%	42%
DJF	0.21	0.8	0.54	0.23	0.7	3.2	1.0	0.4	24%	57%	11%	36%
MAM	0.37	1.9	0.62	0.81	2.7	10.5	5.3	4.1	26%	69%	15%	52%
JJA	0.23	2.3	0.22	0.8	3.9	13.6	7.5	8.3	23%	69%	6%	32%
SON	0.26	1.3	0.52	0.52	1.5	4.2	2.6	2.2	32%	73%	18%	48%

a: Mean over oceanic areas.

b: Maximums over oceanic areas.

c: Ocean areas within 27~40°N, 115~123°E.

d: Ocean areas within 35~55°N, 140~160°E.

Table 9. Modeled domain and annual/seasonal mean near surface wind speed, temperature, precipitation, and relative humidity (RH) over the western Pacific of East Asia (Mean), the EYB region, and the NWP region.

	Wind speed (m s^{-1})			Temperature (°C)			Precipitation (cm month^{-1})			RH (%)		
	Mean ^a	EYB ^b	NWP ^c	Mean ^a	EYB ^b	NWP ^c	Mean ^a	EYB ^b	NWP ^c	Mean ^a	EYB ^b	NWP ^c
ANN	4.3	2.9	4.0	19.2	15.1	8.5	6.1	2.7	8.0	78	73	83
DJF	6.4	4.5	6.9	14.0	4.5	1.0	7.0	1.8	12.4	75	67	77
MAM	3.8	2.0	3.7	16.9	13.4	5.1	4.3	2.1	7.0	79	75	84
JJA	3.0	1.9	2.5	24.0	23.2	15.8	5.1	3.5	3.7	83	80	94
SON	4.1	3.1	3.1	21.7	17.9	12.0	7.9	3.2	9.0	76	71	77

a: Mean over oceanic areas.

b: Ocean areas within 27~40°N, 115~123°E.

c: Ocean areas within 35~55°N, 140~160°E.



Table 10. Modeled regional and annual/seasonal mean all-sky TOA direct radiative effect (DRE) and indirect radiative effects (IRE) due to MOA, anthropogenic aerosols, and sea salt over oceanic areas of the western Pacific (WP), the EYB region, and the NWP region. The units are $W m^{-2}$.

	MOA			Anthropogenic			Sea salt		
	WP ^a	EYB ^b	NWP ^c	WP ^a	EYB ^b	NWP ^c	WP ^a	EYB ^b	NWP ^c
	DRE								
ANN	-0.27	-0.33	-0.50	-2.8	-6.6	-2.7	-0.86	-0.56	-0.89
DJF	-0.18	-0.32	-0.21	-1.2	-3.5	-1.2	-0.93	-0.48	-0.95
MAM	-0.38	-0.34	-0.76	-2.8	-6.2	-3.0	-0.79	-0.36	-1.09
JJA	-0.28	-0.26	-0.72	-4.9	-11.0	-5.0	-0.77	-0.85	-0.79
SON	-0.26	-0.38	-0.32	-2.2	-5.5	-1.4	-0.94	-0.55	-0.73
	IRE								
ANN	-0.66	-0.23	-1.04	-7.7	-4.6	-8.67	-0.41	-0.08	-0.43
DJF	-0.64	-0.28	-0.57	-10.8	-4.8	-9.17	-0.43	-0.06	-0.31
MAM	-0.94	-0.21	-1.40	-9.9	-4.9	-10.65	-0.47	-0.07	-0.58
JJA	-0.36	-0.07	-0.78	-4.5	-3.7	-7.34	-0.30	-0.07	-0.46
SON	-0.70	-0.38	-1.38	-5.7	-5.1	-7.52	-0.45	-0.13	-0.37

a: Mean over oceanic areas.

b: 27~40°N, 115~123°E.

c: 35~55°N, 140~160°E.